UNIVERSITY OF EMBU

SAMUEL NDUNG'U WAITHIRA

MASTER'S OF SCIENCE THESIS

AUGUST, 2024

EFFECTS OF TEMPERATURE, DEFECT, AND pH ON PROPERTIES OF $CaAl_2O_4$: Eu^{2+}, Dy^{3+} PHOSPHOR FOR LIGHTING APPLICATION

SAMUEL NDUNG'U WAITHIRA

A THESIS SUBMITTED IN PARTIAL FULFILLMENT FOR THE DEGREE OF MASTER OF SCIENCE IN CHEMISTRY IN THE UNIVERSITY OF EMBU

AUGUST, 2024

DECLARATION

This thesis is my original work and has not been presented elsewhere for a degree or any other award.

Signature…… Date…….

Samuel Ndung'u Waithira
Department of Physical Sciences
B523/1487/2021

This thesis has been submitted for examination with our approval as the University Supervisors

Signature…… Date…….

Dr. Sharon Kiprotich
Department of Physical and Biological Sciences
Murang'a University of Technology

Signature……Date……

Dr. Ali Halake Wako
Department of Physical Sciences
University of Embu

Signature…… Date…….

Dr. George Simba Nyamato
Department of Physical Sciences
University of Embu

DEDICATION

This work is dedicated to my late grandmother Nyadiri Karoki, my mother Teresiah Waithira, my siblings Joseph and Gabriel, and my uncle Rev. Dominic Njoroge for their prayers and support during my academic journey.

ACKNOWLEDGMENT

♣ Above all, I forward my gratitude to my God, for all the strength He provided me throughout this work.

♣ I am very thankful for the exceptional supervision and support I got from my supervisor Dr. Ali Halake Wako. I also thank him for giving me the chemicals I needed and helping me arrange this work's chapters. If it was not for him, this work would not have been a success.

♣ My gratitude goes to my supervisor Dr. Sharon Kiprotich for her suggestions in this work and manuscripts. Most importantly, I would like to thank her for facilitating characterization of the samples using XRD, FTIR, UV-Vis, and SEM measurements.

♣ I am very grateful to my supervisor Dr. George Simba Nyamato for his supervision, wake up calls, suggestions in this work and with the manuscripts.

♣ My thanks also go to the University of Embu for offering me the scholarship to do my master's degree and Murang'a University of Technology for allowing me to use their muffle furnace and FTIR equipment.

♣ My thanks also go to all staff members of the Physical Sciences department for their support and encouragement.

♣ I would like to also acknowledge all the suggestions that contributed to the success of this work from my fellow researchers.

♣ I am very grateful to Yvonne Kendi for the encouragement and moral support she gave me throughout this work

TABLE OF CONTENTS

Table of Contents

LIST OF TABLES

LIST OF FIGURES

LIST OF ABBREVIATIONS

AAS	Atomic Absorption Spectrometer
BSEs	Backscattered Electrons
CIE	Computer-Integrated Engineering
CL	Chemiluminescence
CT	Calcination Temperature
EDS	Energy Dispersive X-ray Spectrometer
EDXRF	Energy Dispersive X-ray Fluorescence
EL	Electroluminescence
FTIR	Fourier-Transform Infrared Spectroscopy
ICDD	International Center for Diffraction Data
JCPDS	Joint Committee on Powder Diffraction Standards
pH	Potential of Hydrogen
PL	Photoluminescence
SEM	Scanning Electron Microscope
TEM	Transmission Electron Microscope
TL	Thermoluminescence
UV-VIS	UV-VIS- Ultraviolet-Visible
XRD	X-ray diffractometer

ABSTRACT

Electricity is the main source of energy used for lighting but still worldwide, a population of about 1.4 billion does not have any access to electricity, with 85 % of them coming from rural areas. Most of the people in the rural areas use kerosene oil as the main source of energy for lighting which produces smoke that does not only pollute the environment but has adverse health effects on the people. $CaAl_2O_4$: Eu^{2+}, Dy^{3+}phosphor is a very promising source of energy in the future. It is environmentally safe and involves less cost of installation and energy production. Phosphors are solid substances that give off light, a phenomenon known as luminescence and consist of a host matrix and dopants. In this work, effects of synthesis temperature, defect, and pH on both structural and optical properties of $CaAl_2O_4$: Eu^{2+}, Dy^{3+} phosphor were investigated. Europium doped and dysprosium co-doped Calcium aluminate nanomaterial ($CaAl_2O_4$: Eu^{2+}, Dy^{3+}) was prepared using a facile solution combustion technique. Combustion synthesis method is better compared than other conventional methods because of its benefits such as its low synthesis temperature of 500 - 600 °C and its quick processing time. Furthermore, the combustion method is an energy-saving technique that is highly exothermic, and homogenous products are formed within a short time. Similarly, combustion synthesis produces a much smaller grain size compared to alternative conventional approaches. Although the phosphorescence of $CaAl_2O_4$:Eu^2 is known, information about the effect of different dopants and other synthesis conditions is scant. All the synthesized samples underwent characterization employing a range of analytical methods. The findings of X-ray diffraction (XRD) verified that every sample had the monoclinic phase and all the peaks can be matched well with the typical monoclinic $CaAl_2O_4$ peak matching with the ICDD data file (no.069-0033) for orthorhombic structure. The anticipated chemical combustion results of the finished product were provided by the Fourier-transform infrared analysis. The XRD patterns displayed that there was a notable shift to higher 2theta of the prominent peaks diffraction angles with change in synthesis parameters. This is attributed to an increase in particle sizes which led to an increase in lattice parameters. The Debye-Scherrer relation was utilized to ascertain the crystallite sizes of the samples in their prepared state. It was noted that there is variation in the crystallite sizes with synthesis conditions. Analysis of the UV-Vis spectra revealed that the absorption edges also shifted with synthesis parameters. Images captured by a scanning electron microscope revealed that every sample had pores and cracks in an uneven shape. The EDS outcome indicated that the elements of the phosphor for all samples are components of O, Al, and Ca indicating that the phase of final product was actually made of calcium aluminate. The study offers a straightforward path to synthesize $CaAl_2O_4$: Eu^{2+}, Dy^{3+} phosphors with ideal pH, barium concentration, and synthesis temperature generating the sample that exhibits the highest degree of crystallinity suitable for incorporation into lighting fixtures.

CHAPTER ONE

INTRODUCTION

1.1 Background Information

Phosphors are solid materials that emit light, a phenomenon known as luminescence, and maybe a powder or a thin film. This happens when they absorb ultraviolet, visible light, or thermal radiation (Wako, 2011 Ju *et al*., 2014). Luminescence is the radiation released into the visible spectrum. Phosphors consist of a host matrix and dopants. The most common hosts are those of alkaline earth metals for example $CaAl_2O_4$, $BaAl_2O_4$ and $SrAl_2O_4$ while commonly used dopants are rare earth metals like europium (Eu), dysprosium (Dy), and neodymium (Nd).

In 1996, $CaAl_2O_4$: Eu^{2+}, Dy^{3+} was discovered (Matsuzawa *et al.,* 2010) and it's used as a new persistent luminescent compound after which many researchers have come up with some methods for the synthesis of (Calcium Aluminate) powders. The methods included and are not limited to chemical precipitation, hydrothermal synthesis, sol-gel method, and solid-state reaction. Nevertheless, these techniques exhibit numerous significant limitations, including the need for elevated synthesis temperatures, typically between 1300 °C and 1500 °C, and extended processing durations. Additionally, the resultant powders tend to possess substantial grain sizes, adversely influencing the luminescent properties that are critically contingent upon the grain size. Due to these limitations, combustion synthesis was adopted and preferred. The combustion synthesis method is better for obtaining these phosphorescent materials due to some advantages like low processing temperature of 500 °C - 600 °C and fast synthesis. Similarly, this method produces a submicron grain size. The combustion synthesis method is better compared to other conventional methods because of its benefits such as its low synthesis temperature of 500 - 600 °C and its quick processing time. Similarly, combustion synthesis produces a much smaller grain size compared to other conventional methods (Song *et al*., 2008). Furthermore, the combustion method is an energy-saving technique that is highly exothermic, and homogenous products are formed within a short time (Abshiro *et al*., 2018).

Studies of phosphorescent materials have been done because of their numerous uses in a variety of industries, including inks, fluorescent lights, clocks, and highway alerts. $CaAl_2O_4$ is said to have a dominant hexagonal structure that remains unchanged even after doping with rare earth metal/lanthanide, Europium ion (Eu^{2+}) (Singh *et al.*, 2016). The long-time used sulphide phosphors are inferior to aluminate (Al_2O_4) phosphors doped with Eu^{2+} dopant (Wako et al., 2014b). The dopant gives a broadband emission spectrum since the dopant undergoes an electronic transition from $4f^6\ 5d^1$ to $4f^7$ (Singh *et al*., 2016). This is because the excited Eu^{2+} ion is very unstable in a changed lattice structure (Wako *et al*., 2014a).

The chemical composition of the precursor and synthesis conditions primarily influences phosphorus's optical and structural characteristics. Temperature is one of the conditions that affect the properties of phosphors. When the temperature is increased, $CaAl_2O_4$:Eu^{2+} phosphors will emit radiation through thermoluminescence (TL) which will occur at different regions of different temperatures. This is in close relation to its long persistent luminescence properties and properties of photo-stimulated luminescence. Besides electrons in these temperature traps can be re-trapped once more, hence persistent photo-stimulated luminescence (He *et al.*, 2015).

Alkaline-earth aluminate phosphors exhibit long photoluminescence intensity for a long period and are chemically stable (Mao *et al.*, 2016). It emits maximum spectra, blue in color, at 490-495nm as Eu^{2+} undergoes electron transition (Singh *et al.*, 2016). However, co-doping done using other ions of the rare earth metal group leads to emission spectra within the green region at a maximum wavelength of 500nm (Sakai *et al*., 1999, Bartwal *et al*., 2008). The co-doping of $CaAl_2O_4$:Eu^{2+} phosphor with other ions of the rare earth metal group generates deeper traps, hence longer afterglow phosphorescence (Ryu *et al*., 2008).

1.2 Statement of the Problem

Electricity is the main source of energy used for lighting but around the world, approximately 1.4 billion individuals still lack a supply of electricity, with 85% of them coming from rural areas (Kaygusuz *et al*., 2012). Most people in rural areas use kerosene

oil as the main energy source for lighting, producing smoke that not only pollutes the environment but has adverse health effects on the people (Chandan *et al*., 2014). Solar energy is used as a source of energy but it is expensive to install the solar system as the solar panels and storage batteries need to be frequently replaced. Zinc Sulphides phosphors (ZnS;Cu) have been used as luminescent materials but due to their very short decay time, they are doped with radioactive isotopes to improve luminescence, which makes them harmful. This made the use of this type of phosphor prohibited hence there was a need to replace those (Wako *et al*., 2011).

Phosphor materials have been observed to give different intensities at different synthesis conditions. Although the phosphorescence of $CaAl_2O_4$:Eu^{2+} is known, information about the effect of different dopants and other synthesis conditions is scant. Still, no evidence of the optimum temperature and pH can provide a long afterglow nanomaterial. There is need to determine the influence of synthesis temperature, pH, and, Barium and Neodymium defects on the structure and optical properties of $CaAl_2O_4$: Eu^{2+}, Dy^{3+} nanoparticles.

1.3 Justification

Phosphors can be used as efficient sources of energy applicable in lighting. They have also been incorporated into sportswear reflectors, plasma display panels (PDPs), and White Light light-emitting diodes (WLEDs). They are believed to improve energy storage efficiency, hence a major focus at the moment. They can also be applied to solar panels to improve energy output as they transform thermal energy into light energy.

Energy is very essential and it is in the interest of this study to provide efficient energy in a form that is environmentally safe and at an economical cost. Calcium aluminate phosphor ($CaAl_2O_4$:Eu^{2+}) phosphor is an up-and-coming source of energy in the future. It involves less cost of installation and energy production. Furthermore, phosphors have a wide range of applications in emergency guidance during intentional blackouts, in light emitting devices, fluorescence lamps, watches, and demarcation of loads even though their studies are limited (A. H. Wako *et al*., 2014, 2016; Yen *et al*., 2018). Better and long-lasting emissions were achieved by studying this phosphor in a more detailed manner. This will help lighting that is less reliant on electricity. Compared to Zinc

Sulphides phosphors (ZnS;Cu) which are doped with radioactive isotopes, $CaAl_2O_4$ was doped with rare earth metals which makes them environmentally friendly.

1.4 Null Hypothesis

H_{01}: The combustion method does not alter the characteristics of $CaAl_2O_4$: Eu^{2+}, Dy^{3+} phosphor.

H_{02}: Synthesis temperature has no effect on the structure and optical properties of $CaAl_2O_4$: Eu^{2+}, Dy^{3+} nanoparticles.

H_{03}: pH variations do not affect the structure and optical properties of $CaAl_2O_4$: Eu^{2+}, Dy^{3+} nanoparticles.

H_{04}: The introduction of Barium and Neodymium defects in the host matrix of $CaAl_2O_4$: Eu^{2+}, Dy^{3+} nanoparticles does not influence their structure and optical properties.

1.5 Objectives

1.5.1 General Objectives

To study the influence of growth temperature, defects in a host matrix, and pH on the structural and optical properties of $CaAl_2O_4$: Eu^{2+}, Dy^{3+} nanoparticles synthesized by combustion method.

1.5.2 Specific Objectives

1. To characterize $CaAl_2O_4$: Eu^{2+}, Dy^{3+} phosphor synthesized by combustion method.
2. To determine the effect of synthesis temperature on the structure and optical properties of $CaAl_2O_4$: Eu^{2+}, Dy^{3+} nanoparticles.
3. To determine the effect of pH on the structure and optical properties of $CaAl_2O_4$: Eu^{2+}, Dy^{3+} nanoparticles.
4. To determine the influence of Barium and Neodymium defects in the host matrix of $CaAl_2O_4$:Eu^{2+}, Dy^{3+} nanoparticles on the structure and optical properties.

CH APTER TWO

LITERATURE REVIEW

2.1 Introduction

The phenomenon known as luminescence is the process by which excited phosphor material slowly emits stored radiation in the visible region at room temperature (Aitasalo *et al*., 2006). $CaAl_2O_4:Eu^{2+}$, Dy^{3+} is a phosphor material that exhibits luminescence properties. If light absorption excites the material, the phenomenon is known as thermal luminescence (TL) (Aitasalo *et al*., 2006). The workings of persistent luminescent of $CaAl_2O_4:Eu^{2+}$, Dy^{3+} and $SrAl_2O_4:Eu^{2+}$, $Dy^{3+,}$ was first proposed by Matsuzawa (Dorenbos, 2005). Compared to conventional sulfide-based phosphors, calcium, strontium, and barium-based phosphors possess safe, bright, and long-lasting afterglow. Furthermore, these phosphors are chemically stable and therefore do not decompose easily. To enhance the qualities of luminescence of these sulfured–based phosphors, radioactive dopants were used which are now prohibited (Kaya *et al*., 2010; Wako *et al*., 2014a). Doping of inorganic phosphors with rare earth metal lanthanides increases their luminescence properties and also helps them to show broadband emission. This makes these phosphors suitable for many industrial applications including but not limited to, emergency guidance during intentional blackouts, light emitting devices, fluorescence lamps, watches, demarcation of loads, and radiation dosimetry (Wako *et al*., 2014b, 2016; Yen *et al*., 2018). The luminescence property of Eu^{2+} doped and Dy^{3+} co-doped $CaAl_2O_4$ is attributed to the allowed transition of Eu^{2+}ion and enhanced by the formation of deeper traps caused by Dy^{3+}ion.

Many methods have been used to synthesize phosphor material including the sol-gel method (Hasnidawani *et al*., 2016), solid-state reaction (Qiao *et al*., 2009), co-precipitation method, and solution combustion method. Compared to other methods, the solution combustion method helps to control the amount of each component, gives a uniform mixture, needs a low synthesis temperature, and takes a short time (Wako *et al*., 2014).

2.2 Types of luminescence

2.2.1 Chemiluminescence

Chemiluminescence (CL) occurs when photons are emitted as a consequence of a chemical reaction. This happens when a chemical reaction yields an electronically excited intermediate or product (Campbell *et al*., 1988). Research on the spectral and kinetic properties of the heterogeneous chemiluminescence that has been excited by the sulfur dioxide product reveals that chemiluminescence happens during the exchange of atoms and molecules as well as during the adsorption, deposition, and oxidation of reagents (Styrov *et al*., 2014).

2.2.2 Phosphorescence

Phosphorescence is a phenomenon of delayed luminescence that occur when the excited electrons in a triplet state fall back to the ground state as demonstrated by the Jablonski diagram Figure 2.1(Baryshnikov *et al*., 2017). Phosphorescence is delayed due to spin-forbidden transformation (Kuno *et al*., 2015). In this phenomenon, the excited electrons have the same spin orientation as the ground-state electrons (Lakowicz, 1999).

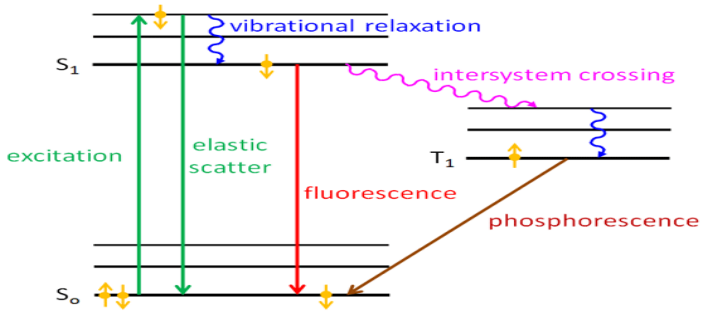

Figure 2.1: Jablonski diagram showing some types of luminescence (Valeur et al., 2011).

2.2.3 Fluorescence

Florescence is the process by which excited electrons returning from an excited singlet state undergo a process of relaxation, ultimately returning to the ground state releasing energy. The second orbital in the ground state and the excited singlet state orbitals in fluorescence have opposite spins. (Valeur *et al*., 2011). The transition in florescence is allowed and hence fast.

2.2.4 Electroluminescence

Electroluminescence (EL) is an emotion of light in the presence of an electric current (Cirio *et al*., 2016).

2.3 Synthesizing of Phosphors

Researchers have come up with many methods for the synthesis of phosphor materials. These methods incudes microwave-assisted chemical precipitation method for the synthesis of $CaAl_2O_4:Eu^{2+},Nd^{3+}$ (YU *et al*., 2017), Sol-gel method which was adopted in the synthesis of $Ba_2SiO_4:Sm^{3+}$ (Zahedi *et al*., 2018), hydrothermal synthesis method used in the synthesis of $Bi_4Ge_3O_{12}$: Eu^{3+} phosphors (Chu *et al*., 2017) and solid -Sate reaction method (Huang *et al*., 2020). In this study, the solution combustion technique was utilized as the method of choice for synthesis of $CaAl_2O_4:Eu^{2+}$, Dy^{3+} .Compared to other methods, combustion method help to control the amount of each component ,give uniform mixture, needs low synthesis temperature and takes short time (Wako *et al*., 2014).

2.4 Influence of Doping

To improve the qualities of luminescence and lengthy afterglow of $CaAl_2O_4$, Eu^{2+} and Dy^{3+} ions are used (Rosticher *et al*., 2015).To explain the cause of these properties, trap and hole mechanisms have been adopted. In the trap mechanism, the allowed transition between the $4d^65f^1$ excited state to $4d^7$ ground state of Eu^{2+} is responsible for the luminescent emission observed. Eu^{2+} forms shallow trap below the conduction band and when electrons are excited, they are promoted to the conduction band then trapped in the shallow traps (Yan *et al*., 2011) as depicted in Figure 2.2 below. The host material can also have intrinsic traps which can sometimes trap electrons (Xue *et al*., 2017). These inherent traps develop throughout the synthesis process as gases escape. Ca^{2+} ions can be substituted by Eu^{2+} and Dy^{3+} ions because they have similar ionic radii. This substitution leads to the disruption of the charge balance causing formation of cationic vacancies where electrons are captured to maintain the charge neutrality (Rodríguez Burbano *et al*., 2015). Introducing the Eu^{2+}ions as a dopant in the host material will result in the creation of shallow traps beneath the conduction band where electrons can be trapped and re-trapped increasing the luminescence persistence. Adding Dy^{3+} as a co-

dopant, will lead to formation of intermediate traps and deeper traps which can capture more electrons and hence leading to longer afterglow of the phosphor (Rodríguez Burbano *et al*., 2015).

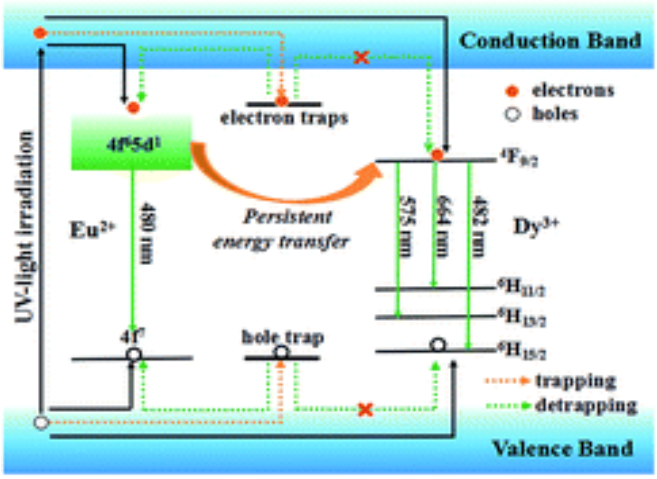

Figure 2.2: Mechanism of luminescence based on electron traps of Eu^{2+} and Dy^{3+} (Yan et al., 2011).

In the hole mechanism illustrated in Figure 2.3, the luminescence property of phosphors is attributed by the release of a hole from the $4d^6 5f^1$ excited state of Eu^{2+} to valence band followed by being trapped by Dy^{3+}. During the day, Eu^{2+} absorbs light and get excited from 4f ground state to 5d excited state. This leads to a release of a hole on 4f to the valence band. This hole then migrates through the valence band until it is trapped by Dy^{3+}. During the nighttime (when the light is withdrawn), the release path is followed which is responsible for the luminescence observed (Dorenbos, 2005; Stefani *et al*., 2009).

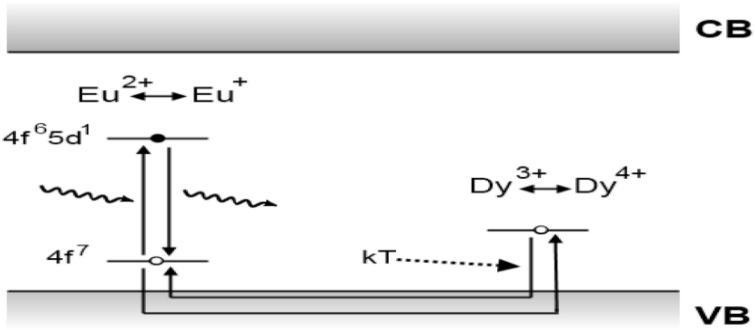

Figure 2.3: Mechanism of luminescence based on hole release (Xu & Tanabe, 2019).

From the two mechanisms proposed above, there must be allowed transition of Eu^{2+} for the luminescence to be observed, in addition, Dy^{3+} increase this luminescence property.

2.5 Influence of Synthesis Temperature

In order to look into the influence exerted by growth temperature on structural and optical characteristics of $CaAl_2O_4:Eu^{2+}$, Dy^{3+}, the phosphor was characterized at different calcination temperature (CT). From previous research It has been reported that at temperature of 500 ^oC the crystals will have appeared (Wako *et al*., 2014). The emission wavelength position of phosphor synthesized by combustion method is not affected by a change in calcination temperature. Consequently, the emission intensity increases between the calcination temperature ranges of 500 - 800 ^oC. The increased emission intensity may be attributed by the enhanced phosphor crystalline (Ekambaram et al., n.d.). However, calcination temperature beyond 1000 ^oC does not affect the intensity of the phosphor's emission.

At different calcination temperature, the morphology and weight of $CaAl_2O_4:Eu^{2+}$, Dy^{3+} will change. The change in the phosphor morphology is attributed by the escaping gases during the synthesis. At higher calcination temperatures (above 700 ^oC) the functional group may be lost. In a research done by , (YU *et al*., 2017) the XRD The findings demonstrated that the degree of crystallinity rises as the temperature rises and at high temperature there was phase changes of the crystal. High synthesis temperature will affect the crystallinity of the final product as the ignition occurs very fast leading to presence of residual water during combustion hence lowering the flame temperature. At very low furnace temperature (below 500 ^oC), the gases will escape slowly marking it difficult for the combustion to take place.

2.6 Effects of pH Variation

In order to vary the pH of the phosphor, ammonia solution or ammonium carbonate $(NH_4)_2CO_3$ was used. Ammonium carbonate was used because in this high furnace temperatures, ammonium carbonate will decompose to ammonium gas and oxides of carbon hence not affecting the purity of the final product. PH affects the preferential precipitation of the phosphor at low pH for example, there is no complete combustion

and hence the Ca and Al will not be completely precipitated giving rise to poorly developed crystal impurity alongside the pure crystal. In a research done by (Shafia *et al*., 2014), on $SrAl_2O_4$: Eu^{2+}, Dy^{3+} phosphor, it was noted that at pH of around the 3-5, there is complete combustion and pure crystal was formed. At very high pH, there was preferential precipitation of aluminum oxohydroxide in the precursor's solution owing to the formation of impurities. It is worth noting that at neutral pH aluminum trihydroxide (Al $(OH)_3$) starts to precipitate, and at certain conditions also, water molecule was lost from aliminium trihyroxide forming AlO(OH) leading to poor homogeneity and formation of suitable complex at high pH. The Phosphorus luminescence characteristics are heavily influenced by pH. The excitation intensity slowly increases with increase in pH (Hsu & Lu, 2009a). PH variation in a great extent affects the morphology of the sample which in turn affects the luminescence properties and hence affecting the application suitability in different fields (Kumar *et al*., 2018). Although the phosphorescence of $CaAl_2O_4$:Eu^{2+} is known, information about the effect of pH is scant

2.7 Influence of Defects in the Host Matrix

The four main crystal defects are line defect, point defect, volume defect and surface defect. Point defects are defects that only occur at a single point in the lattice of a crystal. An atom can be missing from the original crystal lattice, this will cause stress to the neighboring atoms leading to a decrease in the density of the solid due to the reduction of atoms in the crystal lattice as shown in Figure 2.4 (a). This type of defect is called vacancy point defect (Gao *et al.*, 2017). Another type of point defect is one in which an impurity atom assumes a position that was intended for the original atom to occupy as shown in Figure 2.4 (b). The new atom can be of the same or different size from that of the parent atom. This type of defect is known as a substitutional point defect. When an extra atom occupies an interstitial position of a crystal lattice as depicted in Figure 2.4 (c) below, it causes an interstitial point defect (Colen *et al*., 2015).

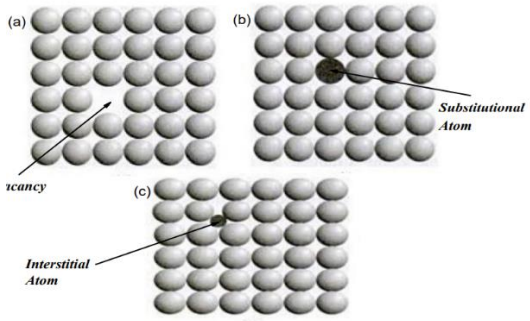

Figure 2.4: Image illustrating types of point defect (Colen *et al.,* 2015).

In a research done by Park and Vogt when comparing the photoluminescence of $Sr_{3-x}A_xAlO_4F$(A = Ca and Ba), it was observed that the broad-band emissions were higher with A = Ba than Ca substituted phosphor. The rejoining of localized electron-hole pairs associated with an O_{2p}-Ba_{5d} transition of BaO_7 is related to this enhanced broad-band emission. In addition, since Ba is bigger than Ca,AlO_4 present in the AO_8F_2 clusters in these layered phosphors will also be affected by a stronger distortion when in the presence of a bigger Ba (Park & Vogt, 2010). There is little information on Barium defect in the host matrix of $CaAl_2O_4$: Eu^{2+}: Dy^{3+} and its research is, therefore, necessary.

2.8 Characterization

To study the structure and the optical characteristics of $CaAl_2O_4$:Eu^{2+}, Dy^{3+} nanomaterial produced through the process of combustion, UV-Vis, FTIR, SEM, AAS, EDXRF, and XRD were used.

2.8.1 Scanning Electron Microscopy (SEM)

Scanning electron microscopy (SEM) is an instrument used for chemical composition characterization and morphology analysis of microstructures (Zhou *et al*., 2006.). For an image to be formed in the SEM, there must be the acquisition of signals produced by the electron beam and interaction of the analyte (Gillam *et al*., 1999). The most important signals in SEM are those which are produced by secondary electrons and backscattered electrons. The analyte atom becomes ionized when primary radiation comes into contact with the sample's surface and here electrons that are not tightly bounded can be emitted which are known as the secondary electrons. Since the secondary electrons are of low energy, they indicate where the beam is located and gives the topographic information

(roughness and surface structure) of the analyte. However, backscattered electrons (BSEs) are produced when the electrons undergo elastic collision with the atomic nucleus of the sample causing the electrons to bounce back (Zhou *et al*., 2017). Elements with a high atomic number have more positive charge in their nucleus and hence more electrons are backscattered. The backscattered electrons produce an image in SEM which is used in the determination of both the sample topographic information as well as what makes up the sample.

SEM is made up of an electron gun that generates electron beams and propagates them to electromagnetic lenses which focus the electron beam produced by the electron gun and form a small, enhanced, and focused sport of electron on the sample which is placed on a sample holder, a signal detector detects the signal from the sample and interpreted by a read out as an image as shown in Figure 2.5 below (Gillam *et al*., 1999; McMullan *et al*., 1995; Mohan *et al*., 2016; Zhou *et al*., 2006.).

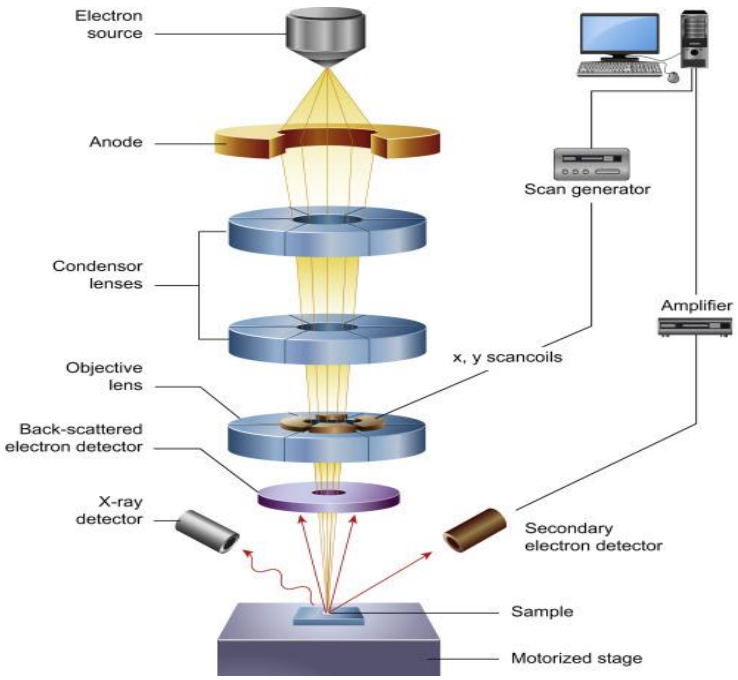

Figure 2.5: A schematic diagram of scanning electron microscope (SEM) (Zhou et al., 2006).

2.8.2 X-ray Diffraction (XRD)

XRD is yet another important analytical instrument that has found application in academic research and also in industry. XRD is employed to characterize crystalline

materials. It gives details on the preferred texture, phase, and the structure of a crystal. X-ray diffraction produces peaks that are as a result of constructive interference between the monochromatic beam of X-ray incident right and the crystalline sample (Bunaciu *et al*., 2015). The distribution of atoms within the sample lattice helps in determination of peak intensities produced by XRD. Figure 2.6 (a) and Figure 2.6 (b) illustrate X-ray diffraction which consists of a cathodic ray tube that produces X-rays, then passed to a filter to produce monochromatic radiations, concentrated, and then to a sample in a sample holder. When this monochromatic X-ray incident radiation strikes the sample, the electrons in the sample crystal vibrate with the same regularity as the occurrence ray and then accelerate. The accelerated electrons emit radiations of similar frequency to that of the incident monochromatic X-ray. A detector picks up these radiations and then interprets as spectra by a readout (Bunaciu et *al*., 2015; Pifferi et *al*., 2009).

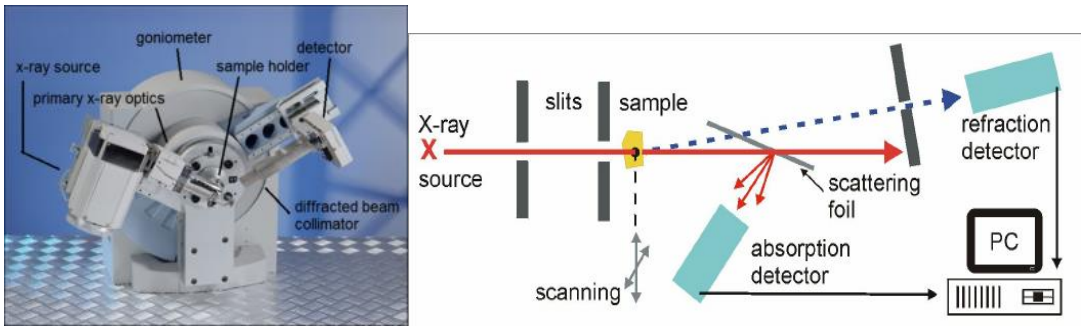

(a) **(b)**

Figure 2.6: Schematic diagram of X-ray diffraction (XRD) (Bunaciu et al., 2015; Pifferi et al., 2009).

2.8.3 Fourier-Transform Infrared Spectroscopy (FTIR)

Fourier-transform infrared spectroscopy (FTIR) is a sophisticated analytical technique employed for the determination of the quality or consistency of a sample, amount of components in the sample, and also to determine the unknown material (Vlachos *et al*., 2006). FTIR Spectrometer consists of a radiation source falling within the IR region (far, mid, and near), an interferometer as the wavelength selector, a sample holder, and a detector. The interferometer consists of a beam splitter, a laser beam, a fixed, and a moving mirror. The beam splitter receives radiation from the source, diverging it into

two beams, whereby one traverse towards the immobile mirror while the other advances towards the mobile mirror. The beams are then reflected and reinforced directed to the sample. The intensity of light can be measured at different lengths of the moving mirror and hence optical path difference is obtained which produces interference to the spectra (either constructive or destructive). The results obtained can be used to plot a spectrum representing molecular absorption and transmission and create a molecular fingerprint (Wako *et al*., 2014).

2.8.4 UV-VIS Spectroscopy

UV-VIS Spectroscopy is a tool for analysis that quantifies the amount of UV- light transmitted through or absorbed by a sample. The information is then used to plot an absorbance spectrum of the sample. Using Beer Lambert law, the concentration of the analyte can also be determined. The primary elements of a UV-vis spectrometer consist of a light source that generates the UV light, a sample holder where the sample is placed usually a cuvette, a wavelength selector, and a detector (Picollo *et al*., 2019).

Chapters 3-6 describe the results of the work done to gain insight into the influence of synthesis temperature, pH, and, Barium and Neodymium defects on the structure and optical properties of $CaAl_2O_4$: Eu^{2+}, Dy^{3+} nanoparticles, while the overall conclusions and recommendations are summarized in chapter 7.

CHAPTER THREE

SYNTHESIS AND CHARACTERIZATION $CaAl_2O_4$: Eu^{2+}, Dy^{3+} PHOSPHOR SYNTHESIZED BY COMBUSTION METHOD

3.1 Synthesis method

Eu^{2+} doped and Dy^{3+} co-doped calcium aluminate phosphor was synthesized using the solution combustion method as adopted by Ekambaram *et al*., n.d.; A. H. Wako *et al*., 2014, and Yang *et al.*, 2021 with slight modification. The starting material consisted of analytical pure grade $Al(NO_2)_2 \cdot 9H_2O$, $Ca(NO_2)_2$, $Dy(NO_3)_3$, $Eu(NO_3)_3 \cdot 5H_2O$ and urea ($CO(NH_2)_2$) as the fuel all obtained from MERCK in analytical purity of 99.9% and used as received (Wako *et al*., 2014). The antecedents were made using Ca/Al ratio kept constant at 1:2 mol% according to stoichiometric ratio. The levels of doping with Eu^{2+} and Dy^{3+} were also kept constant at optimum concentration. Using magnetic stirrer, the precursors were mixed for 15 minutes in deionized water to achieve a uniform outcome. Next, the mixture was transferred into crucibles introduced into a muffle furnace, and synthesized at a furnace temperature of 500°C as illustrated in Figure 3:1.

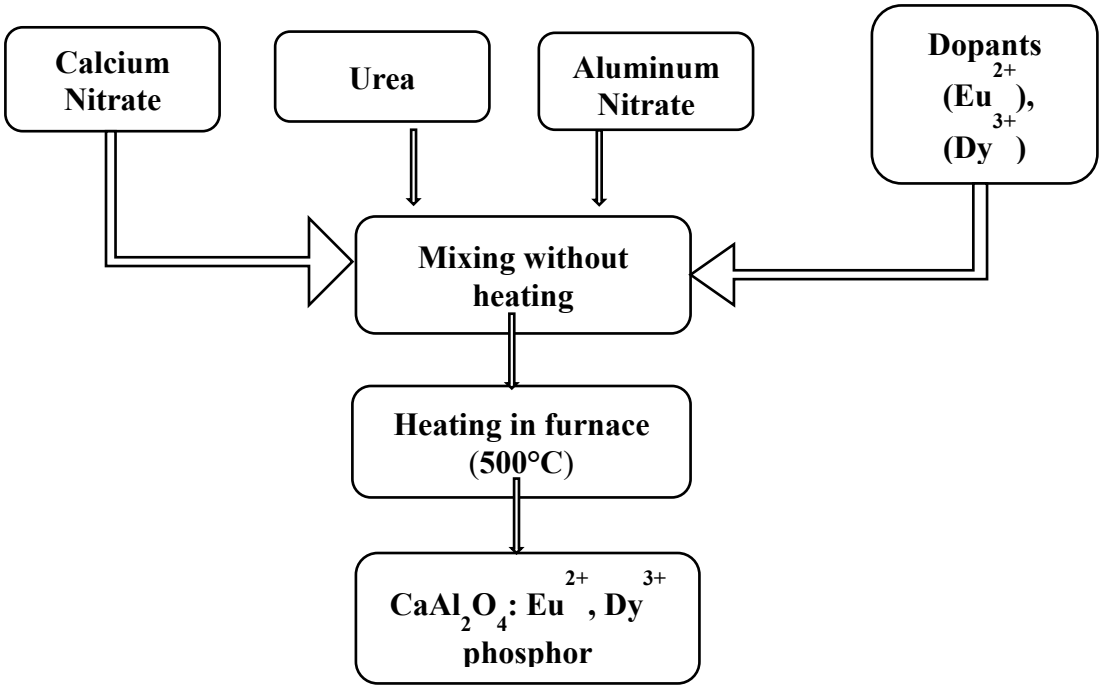

Figure 3.1: Flow diagram for the synthesis of CaAl2O4: Eu^{2+}, Dy^{3+} phosphor

The solution boiled then evaporated and decomposed with the release of gases (oxides of nitrogen, carbon, and ammonia) smoke, and fumes. After spontaneous ignition, combustion ensued, characterized by substantial volumetric expansion and the formation of white foam. This resultant foam was allowed to cool to ambient temperature, after which it was subjected to milling processes to produce the final product, as depicted in Figure 3.2.

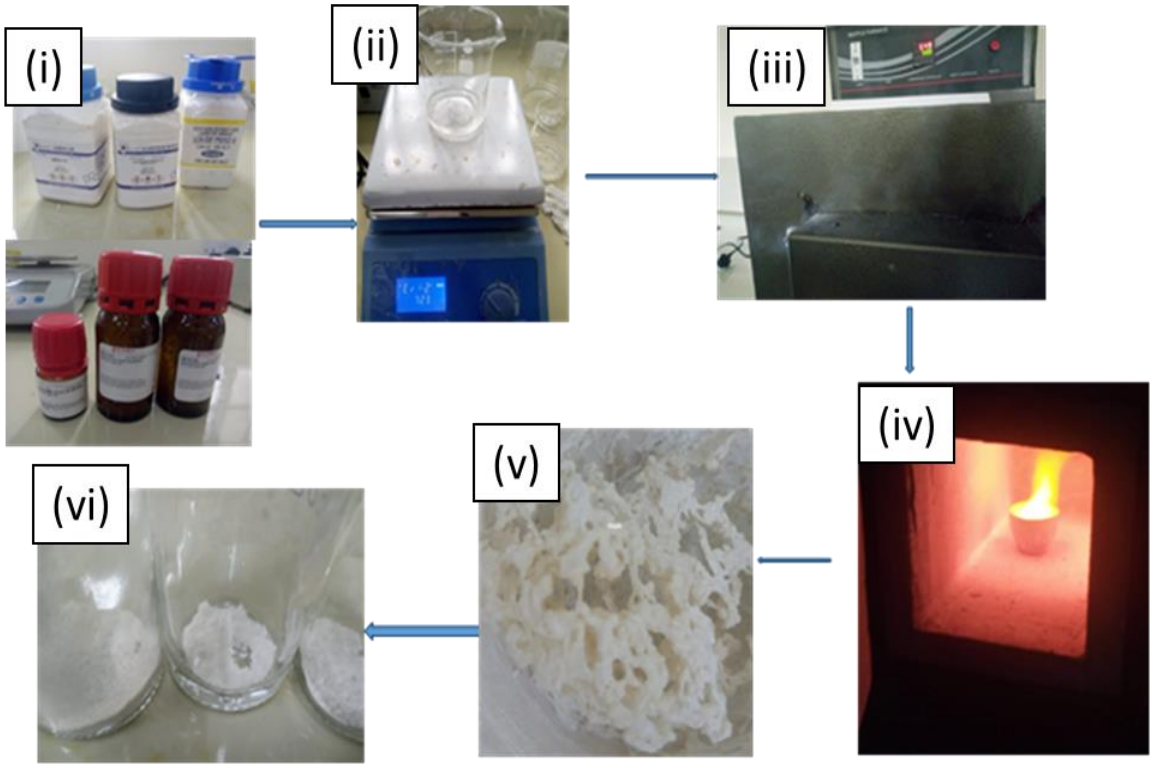

Figure 3.2: Schematic diagram for synthesis and final product of $CaAl_2O_4$: Eu^{2+}, Dy^{3+} phosphor synthesized by combustion method**.**

The samples were further characterized by employing a variety of analytical methods. JEOL JSM-7500F field emission scanning electron microscope (FE-SEM) was used to explore the product particles' morphologies. The UV-Vis absorption spectra of the phosphor material were recorded using a Perkin-Elmer Lambda 750s UV-Vis spectrometer. The crystallinity and phase of the samples were examined using an X'Pert PRO PANalytical XRD diffractometer, utilizing Cukα radiation with a wavelength of λ = 0.15405 nm to obtain the samples' X-ray diffraction (XRD) spectra. The consistency

of the sample components and the type of bonds present in the sample were investigated using an FT-IR360 infrared spectrometer with KBr pellets, covering the spectral range from 4,000 to 400 cm−1.

3.2 RESULTS AND DISCUSSION

3.2.1 Fourier Transform Infra-Red Analysis

The consistency of Fourier-transform infrared spectroscopy was used to examine the sample's constituent parts and the kinds of bonds that were found there. Figure 3.3 shows the FTIR spectra of $CaAl_2O_4$: Eu^{2+}, Dy^{3+} phosphor synthesized by combustion method.

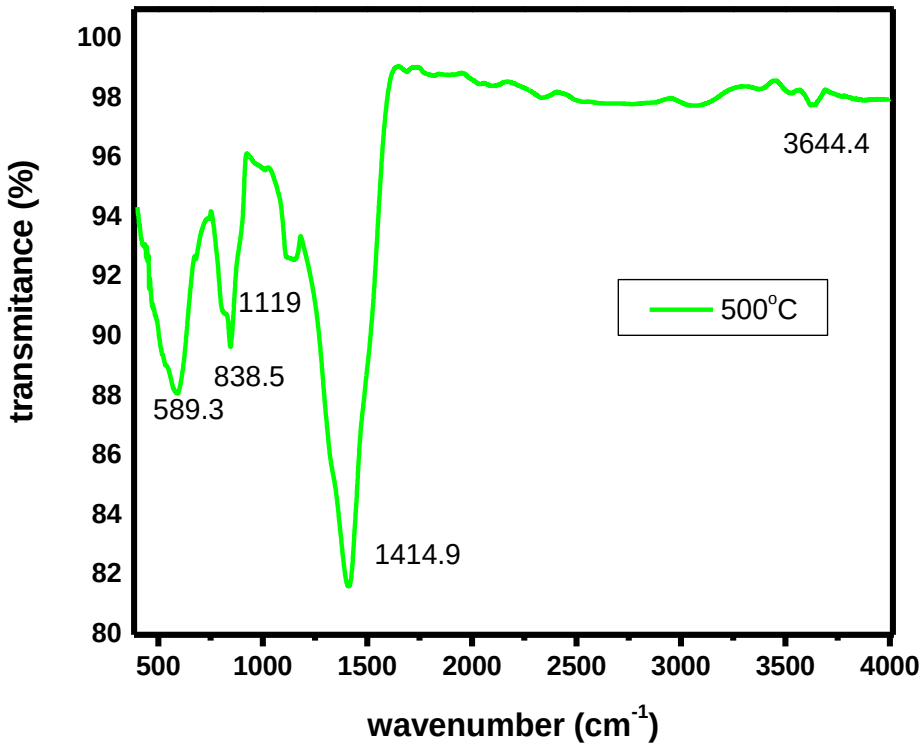

Figure 3.3: FTIR spectra of $CaAl_2O_4$: Eu^{2+}, Dy^{3+} phosphor synthesized by combustion method.

The band at 589.3 cm^{-1} represents the absorption band of AlO_6, while the band at 838.5 cm^{-1} is associated with the stretching vibration of AlO_4 implying that significant bands of $CaAl_2O_4$ are identified in the spectrum (Karacaoğlu, 2022). The spectral band located at 1414.9 cm^{-1} is ascribed to nitrate vibrations, consistent with the characteristic region

between 1250 and 1650 cm^{-1}, signifying the formation of intermediates during the synthesis process (Kumara *et al.*, 2016). Furthermore, the absorption band at 3644.4 cm^{-1} is attributed to the symmetric stretching vibrations of water vapor, which has been adsorbed by the sample from the ambient atmosphere.

3.2.2 X-ray Diffraction Analysis

To characterize the crystal structure of the as-synthesized $CaAl_2O_4$: Eu^{2+}, Dy^{3+}, X-ray diffraction (XRD) measurements were performed. The XRD patterns depicted in Figure 3.4 showcase the dominance of diffraction peaks attributed to the monoclinic phase of $CaAl_2O_4$ within the synthesized phosphor. It is noteworthy that all discernible peaks are in agreement with the characteristic monoclinic configuration of $CaAl_2O_4$ peak matching with the ICDD data file no. 069-0033 for orthorhombic structure.

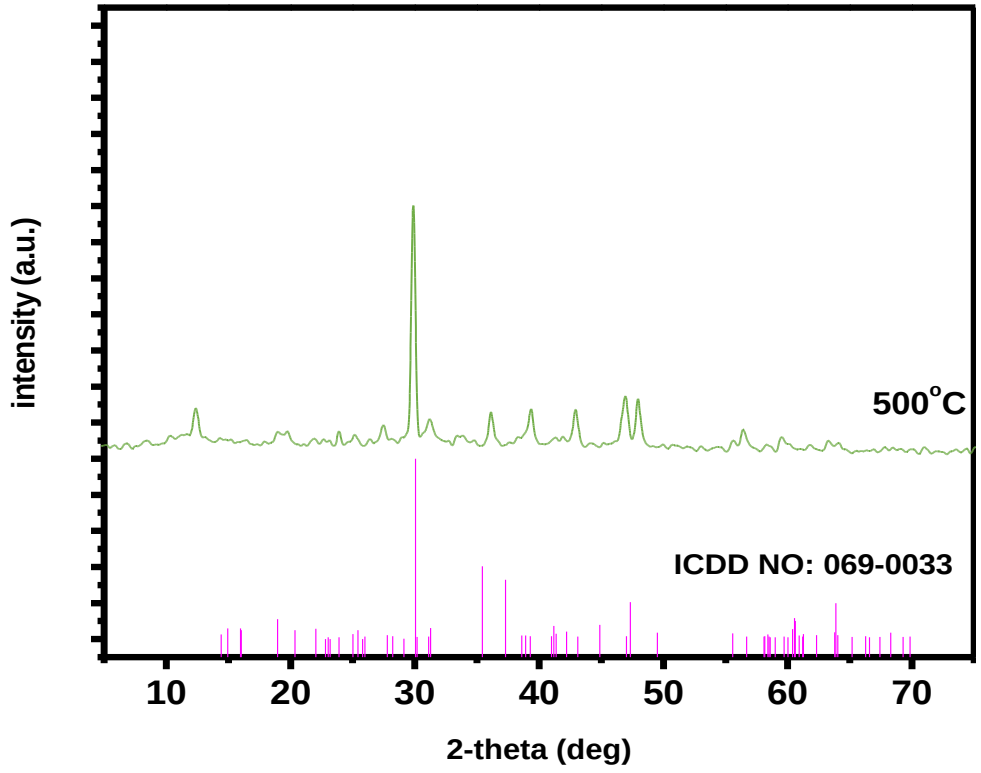

Figure 3.4: XRD patterns for $CaAl_2O_4$: Eu^{2+}, Dy^{3+} phosphor synthesized by combustion method.

Table 3.1. Shows a summary of the peak list. From the table it is seen that the highest peak is located at 2-theta of 29.582 degree and has a height of 1147 cps and a full width at half maximum FWHM of 0.158 degree.

Table 3.1: A summary of peak list for $CaAl_2O_4$: Eu^{2+}, Dy^{3+} phosphor synthesized by combustion method.

No.	2-theta(deg)	d(ang.)	Height(cps)	FWHM (deg)	Int. I(cps deg)	Int. W(deg)	Asym. factor
1	29.582	3.0173	1147	0.158	229	0.20	4.7
2	36.109	2.4854	245	0.07	31	0.12	0.6
3	39.558	2.2763	206	0.11	41	0.20	0.9
4	43.321	2.0869	168	0.15	42	0.25	1.4
5	47.65	1.9069	139	0.44	74	0.53	5
6	48.625	1.8709	231	0.15	63	0.27	1.1

Crystallite size (D) of the product was determined using the Debye-Scherrer's equation (equation (3.1)) (Bertazzo & Bertran, 2006)

$$D = \frac{\kappa\lambda}{\beta \cos\theta} \tag{3.1}$$

where β is the full width at half maximum (FWHM) broadening, θ is the Bragg's diffraction angle, K was the shape factor (0.9), D is the diameter of the crystallite, alongside λ is the emission wavelength of CuKα radiation (0.154 nm) (Farooqi & Srivastava, 2016)**.** From the calculations, the estimated crystallite size was 50.26 nm.

3.2.3 UV-Vis Analysis

The optical properties of the as-prepared $CaAl_2O_4$: Eu^{2+}, Dy^{3+} phosphor synthesized by combustion method was determined using aliquots drawn from freshly prepared samples using a UV-Vis spectrophotometer. The data obtained was used to plot the graphs in Figure 3.5. The absorption edge of $CaAl_2O_4$: Eu^{2+}, Dy^{3+} phosphor produced through the process of combustion was determined to be 263 nm as shown in Figure 3.5.

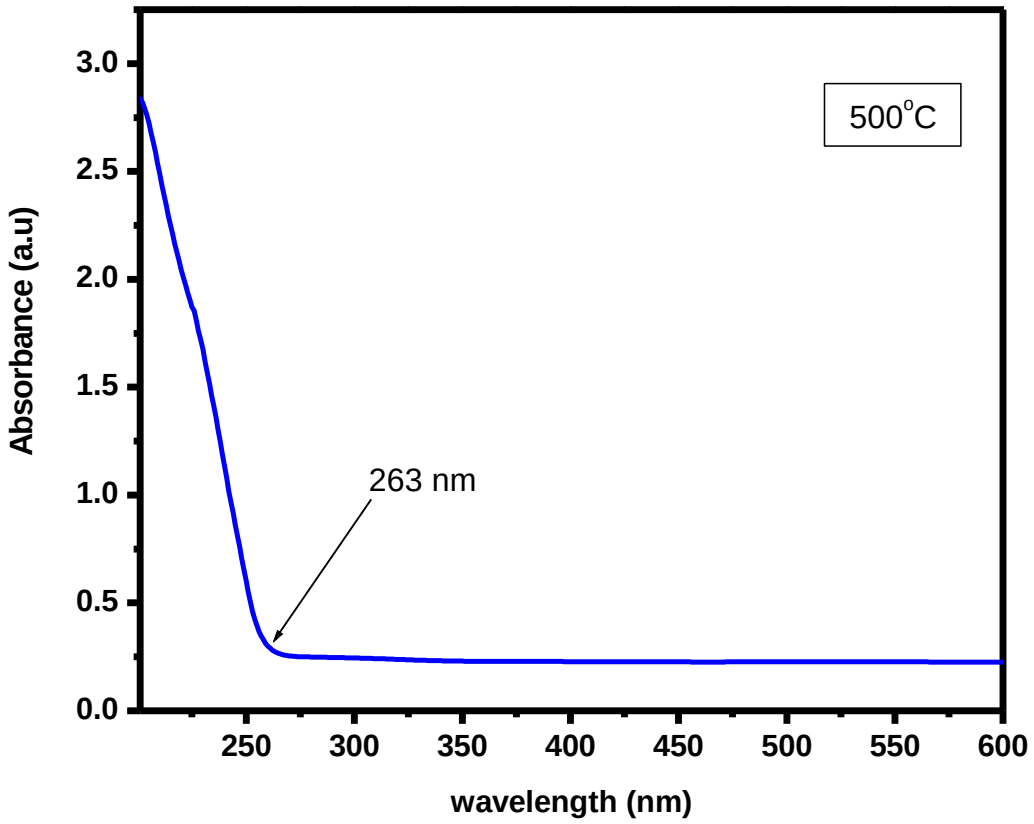

Figure 3.5: UV-Vis spectra plot showing the absorption edge of $CaAl_2O_4$: Eu^{2+}, Dy^{3+} phosphor produced through the process of combustion.

To calculate the optical band gap energy of the as-prepare $CaAl_2O_4$: Eu^{2+}, Dy^{3+} material, Tauc and Daviss-Mott relation (equation 3.2) (Makuła, Pacia, & Macyk, 2018) and Tauc plot (Figure 3.6) were used.

$$(\alpha h\nu)^n = \mathrm{K}(h\nu - \mathrm{E}g) \qquad (3.2)$$

Where K is the energy-independent constant, Eg is the material's optical band gap energy, $h\nu$ is the incoming photon energy, and α is the absorption rate coefficient. In the above equation, the exponent " n " represents the nature of transition (Sangiorgi, Aversa, Tatti, Verucchi, & Sanson, 2017). For materials exhibiting a direct band gap, the power law exponent n is typically assigned a value of 2, while for those with an indirect band gap, n is typically assigned a value of 1/2. In Tauc plot, the band gap energy was estimated by plotting $(\alpha h\nu)^n$ against $h\nu$. The wavelength from the UV-vis spectroscopy was converted to energy and the absorbance coefficient (α) was calculated from

absorbance data. To get $(\alpha h\nu)^n$ plotted in the y-axis, $h\nu$ was taken as incident photon energy and alpha (α) calculated from absorbance data using Beer-Lambert law (equation 3.3) (Swinehart, 1962).

$$\mathrm{I} = \mathrm{I}o e^{-\alpha \iota} \tag{3.3}$$

Where I is the light's transmitted intensity, Io is the light's incident intensity, α is the absorbance coefficient and ι is the length of the path of the light where absorbance occurred.

On the curve, a tangent line where $\alpha = 0$ was then drawn and the location where it makes contact with the x-axis is taken as the optical band gap of the material. The band gap was assessed to be 5.0, as illustrated in Figure 3.6. Consistent observations were documented by Kumar *et al.*, in their study on the adsorption kinetics of hazardous methylene blue from aqueous solutions utilizing combustion-derived $CaAl_2O_4$: Eu^{2+}(Kumara *et al.*, 2016).

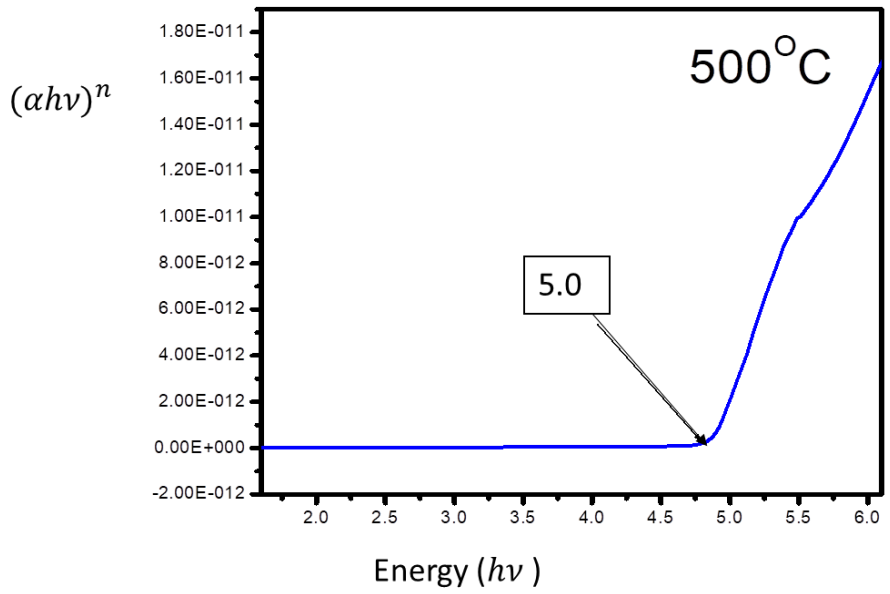

Figure 3.6: Tauc plot for $CaAl_2O_4$: Eu^{2+}, Dy^{3+}phosphor.

3.2.4 Scanning Electron Microscope Analysis

To investigate the morphologies of the product particles, a scanning electron microscope (SEM) was used. The SEM micrographs in Figure 3.7 show that, all the powders are

agglomerated and have an irregular shape with pores and cracks. The cracks and poles may arise from the release of gases during the combustion process, which actively participate in the generation of nano-crystalline material. The process of sintering in the phosphor is circumvented as a result of the dispersion of heat by escaping gases(Colen, 2015). The agglomerates have non-uniform sizes and shapes due to irregular mass flow and non-uniform distribution of temperature during synthesis.

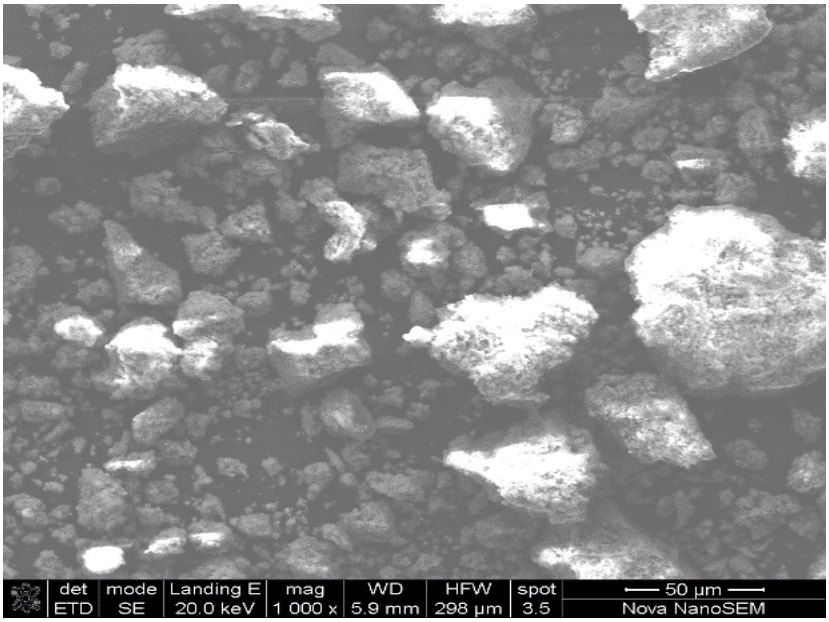

Figure 3.7: SEM images for $CaAl_2O_4$: Eu^{2+}, Dy^{3+} phosphor.

Figure. 3.8 shows the EDS results and spectrum of point spectrum 5. The EDS results and spectrum (Figure 3.8) indicate that the elements present in the phosphor for the sample consisted of O, Al, and Ca indicating that the phase of the final product was made of calcium aluminate. It can be seen that the atomic percentage of all the elements for $CaAl_2O_4$: Eu^{2+}, Dy^{3+} phosphor synthesized at a furnace temperature of 500 °C is close to stoichiometric composition (Figure 3.8 (b)).

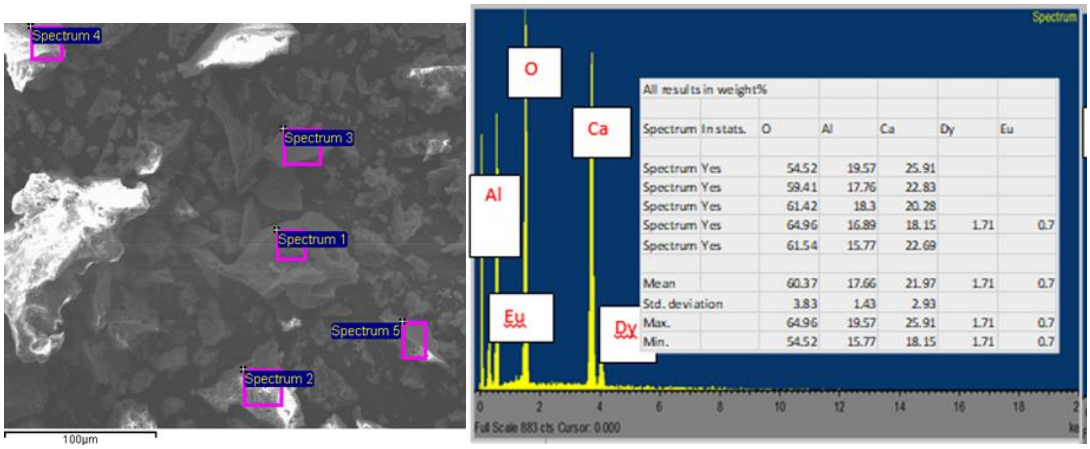

Figure 3.8: SEM image and EDS results from point spectrum 5

3.2.5 Conclusion

The synthesis of $CaAl_2O_4$: Eu^{2+}, Dy^{3+} phosphor using the combustion method was successfully done. The optical and structural characteristics of the as-prepared samples synthesized at different furnace temperatures were analyzed using FTIR, XRD, and UV-Vis spectroscopy. The anticipated chemical combustion results of the finished products were determined from the FTIR analysis. The XRD patterns show that all the major peaks could be indexed to the typical monoclinic $CaAl_2O_4$ peak. The Debye-Scherrer equation was utilized to ascertain the crystallite sizes of the samples in their prepared state, the estimated crystallite size is 50.26 nm. According to the UV-Vis graph, the absorption edge of $CaAl_2O_4$: Eu^{2+}, Dy^{3+} phosphor produced through the process of combustion was determined to be 263 nm. The band gap was estimated to be 5.0. The SEM micrographs show that all the powders are agglomerated and have irregular shapes with pores and cracks. EDS showed that the phase of the final product was made of calcium aluminate.

CHAPTER FOUR

EFFECTS OF SYNTHESIS TEMPERATURE ON THE STRUCTURAL AND OPTICAL PROPERTIES OF $CaAl_2O_4$: Eu^{2+}, Dy^{3+}NANOPARTICLES

4.1. Introduction

Phosphors are solid materials that emit light, a phenomenon known as luminescence, and may also be a powder or a thin film (Rack & Holloway, 1998). This happens when they absorb ultraviolet, visible light, or thermal radiation. Phosphors consist of a host matrix and dopants. The most common hosts are those of alkaline earth metals for example $CaAl_2O_4$, $BaAl_2O_4$, and $SrAl_2O_4$ while commonly used (Parauha, Sahu, & Dhoble, 2021) dopants are rare earth metals like europium (Eu), dysprosium (Dy) and neodymium (Nd).

After the early 1600s saw the discovery of the Bologna stone, persistent luminescence was first described; however, the specifics of the energy storage and gradual release are still poorly explained. Researchers have come up with some methods for the synthesis of (Calcium Aluminate) powders. The methods included and are not limited to chemical precipitation, hydrothermal synthesis, sol-gel method, and solid-state reaction, these methods have many limitations including high synthesis temperatures of around 1300 - 1500 ºC and a long processing time. In addition, the phosphors produced by these methods have a big grain size, affecting the luminescent properties. Due to these limitations, combustion synthesis was used in this study. Because of its benefits, such as its quick synthesis and low processing temperature of 500 – 600 °C, the combustion-based synthesis method is superior. Similarly, This process yields submicron grain sizes (Parauha *et al*., 2021). Furthermore, the combustion method is an energy-saving technique that is highly exothermic, and homogenous products are formed within a short time (Ugemuge, Parauha, & Dhoble, 2021).

Electricity is the main source of energy used for lighting but still Approximately 1.4 billion individuals globally are deprived of access to electrical power with 85 % of them coming from rural areas (Kaygusuz *et al*., 2012). Most of the people in the rural areas use kerosene oil as the main source of energy for lighting which produces smoke that

does not only pollute the environment but has adverse health effects on the people (Chandan *et al*., 2014). Solar energy is used as a source of energy but it is expensive to install the solar system as the solar panels and storage batteries need to be frequently replaced. Zinc Sulphides phosphors (ZnS;Cu) have been used as luminescent materials but due to their very short decay time, they are doped with radioactive isotopes to improve luminescence, which makes them harmful. This made the use of this type of phosphor to be prohibited hence there was a need to replace those (Wako *et al*., 2011).

Energy is very essential and it is in the interest of this study to provide efficient energy in a form that is environmentally safe and at an economical cost. Calcium aluminate phosphor ($CaAl_2O_4:Eu^{2+}$) is an up-and-coming source of energy in the future. It involves less cost of installation and energy production. Furthermore, phosphors have a wide range of applications in emergency guidance during intentional blackouts, in light emitting devices, fluorescence lamps, watches, and demarcation of loads even though their studies are limited (A. H. Wako *et al*., 2014, 2016; Yen *et al*., 2018). Better and long-lasting emissions were achieved by studying this phosphor in a more detailed manner. This will help lighting that is less reliant on electricity. Compared to Zinc Sulphides phosphors (ZnS;Cu) doped with radioactive isotopes, $CaAl_2O_4$ was doped with rare earth metals, making them environmentally friendly. The particles' structural characteristics and size distribution exhibit a strong correlation with both the reaction temperature and the intensity of sonication output power. (A. Esmaielzadeh Kandjani *et a*l.,). Although the phosphorescence of $CaAl_2O_4:Eu^{2+}$ is known, information about the effect of different dopants and other synthesis conditions is scant. This study investigates the influence of synthesis temperature on the structure and optical properties of $CaAl_2O_4$: Eu^{2+}, Dy^{3+} nanoparticles.

4.2. Experimental Procedure

The precursors were prepared with ratios of Ca $(NO_2)_2$ and $Al(NO_2)_2 \cdot 9H_2O$ kept constant at 1:2 mol %. The concentrations of Eu^{2+} and Dy^{3+} dopants were maintained at a constant level of 0.2 mol %. Employing a magnetic stirrer, the precursors underwent a 15-minute mixing process to ensure homogeneity. Subsequently, the homogeneous solution was transferred into crucibles and introduced into a muffle furnace, where a

series of discrete temperatures spanning from 300 °C to 1000 °C were applied. Notably, the synthesis temperature for the control sample was set at 500 °C for comparative purposes. The solution boiled, then evaporated, and decomposed with the combustion causing the release of gases, including oxides of nitrogen, carbon, and ammonia, as well as smoke and fumes. After spontaneous ignition, combustion ensued, accompanied by significant swelling, and white foam was produced. The generated foam was allowed to cool to ambient temperature and milled to form the final product ($CaBaAl_2O_4$: Eu^{2+}, Dy^{3+}, Nd^{3+}).

The samples were further characterized by employing a variety of analytical methods. JEOL JSM-7500F field emission scanning electron microscope (FE-SEM) at South Africa was used to explore the product particles' morphologies. The UV-Vis absorption spectra of the phosphor material were recorded using a Perkin-Elmer Lambda 750s UV-Vis spectrometer at Chuka University. The crystallinity and phase of the samples were examined using an X'Pert PRO PANalytical XRD diffractometer, utilizing Cukα radiation with a wavelength of λ=0.15405 nm. to obtain the samples' X-ray diffraction (XRD) spectra. The consistency of the sample components and the type of bonds present was investigated using an FT-IR360 infrared spectrometer with KBr pellets, covering the spectral range from 4,000 to 400 cm−1 at Murang'a university of technology.

4.3. RESULTS AND DISCUSSION

4.3.1. Fourier Transform Infra-Red Analysis

The figure 4.9 a, b, c, d, e, f and g shows the FTIR patterns of $CaAl_2O_4$: Eu^{2+}, Dy^{3+} synthesized at furnace temperatures of 300 °C, 400 °C, 500 °C, 600 °C, 700 °C, 900 °C and 1000 °C, respectively. In the region 420 cm^{-1} to 690 cm^{-1} , traces of $Ca_3Al_2O_6$ phase are detected(Wako, Dejene, & Swart, 2014). As FTIR is frequently more robust than XRD for evaluating the existence of novel phases, $Ca_3Al_2O_6$ phase traces are not recorded in the XRD data (Phillippi & Mazdiyasni, 1971), while the band of 705 to 860 cm^{-1} are attributed to $CaAl_2O_4$ phase (Fernández-Carrasco, Torrens-Martín, Morales, & Martínez-Ramírez, 2012).

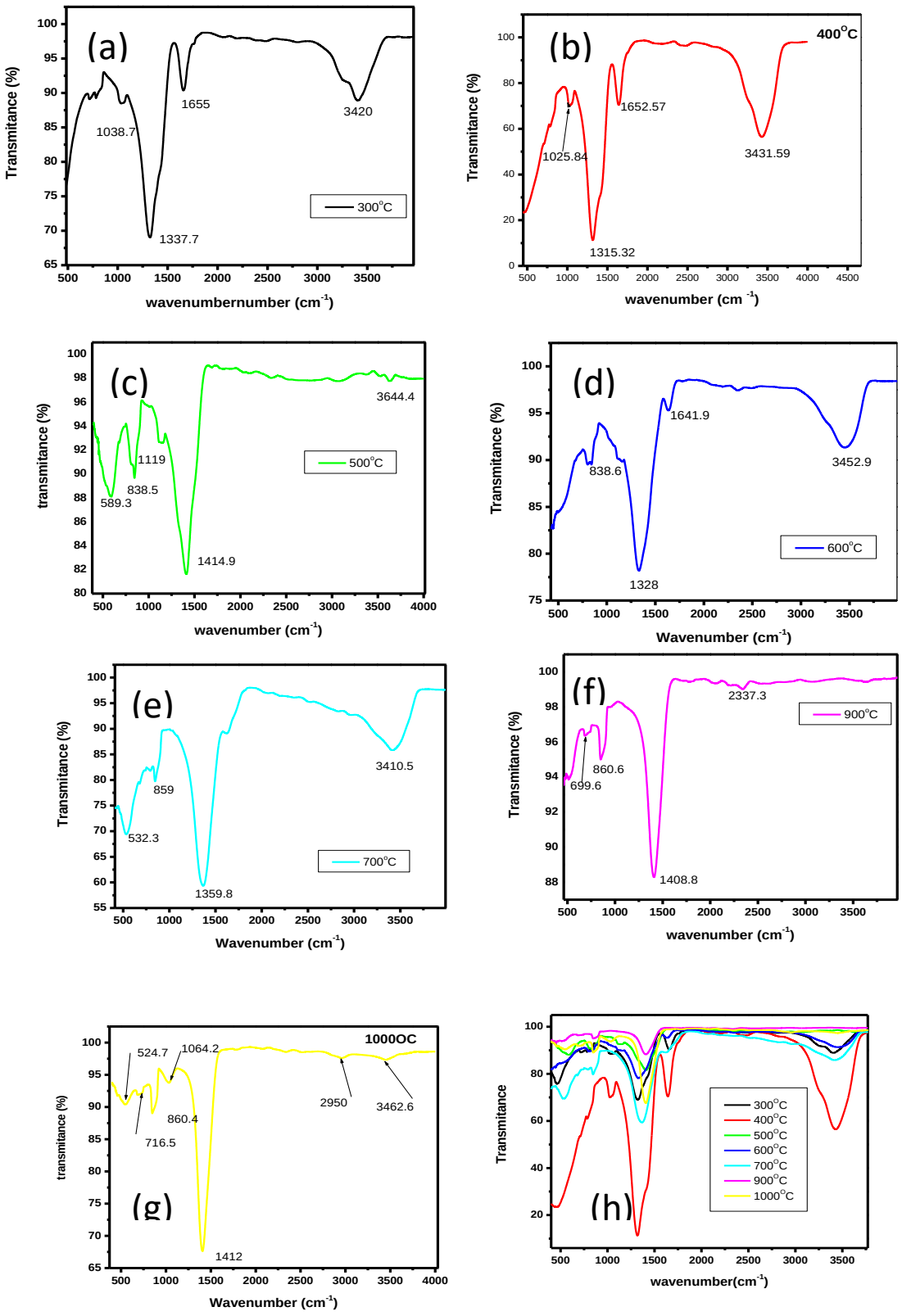

Figure 4.1: FT-IR spectra of $CaAl_2O_4$: Eu^{2+}, Dy^{3+}phosphors synthesized at various furnace temperatures

The absorption band of 3400 cm^{-1} for all the samples is associated to the symmetric stretching vibration of water vapor absorbed by the sample from the atmosphere. This observation aligns with the results documented in the study conducted by Lu *et al*., 2021 (Lu, Shi, Pang, Zhu, & Li, 2021), while the peak observed at 1500 - 1600 cm^{-1} in the infrared spectrum corresponds to the stretching mode of the C=O bond in a carbonyl functional group situated on the crystal surface.

4.3.2. X-ray diffraction Analysis

To get information about the crystal structure of as-prepared $CaAl_2O_4$: Eu^{2+}, Dy^{3+}, x-ray diffraction (XRD) measurements were done. The XRD patterns of $CaAl_2O_4$: Eu^{2+}, Dy^{3+} synthesized at furnace temperatures of 300 °C, 400 °C, 500 °C, 600 °C, 700 °C, 900 °C and 1000 °C are shown in the Figure 4.2. The X-ray diffraction (XRD) patterns of the powders prominently feature diffraction peaks corresponding to the monoclinic phase of $CaAl_2O_4$: Eu^{2+}, Dy^{3+}. All significant peaks observed can be attributed to the characteristic monoclinic phase of $CaAl_2O_4$: Eu^{2+}, Dy^{3+} matching with the ICDD data file (no.069-0033) for orthorhombic structure.

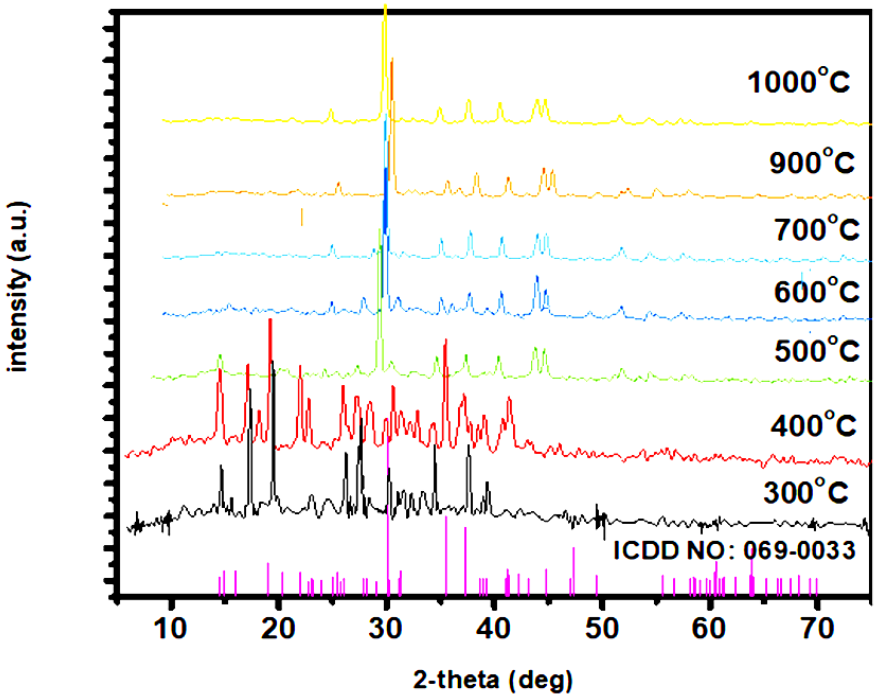

Figure 4.2: XRD patterns for $CaAl_2O_4$: Eu^{2+}, Dy^{3+} phosphor synthesized at different furnace temperatures.

From the XRD patterns, the diffraction angles of the major peaks shift to higher 2theta up to 900 °C. This is attributed to an increase in particle sizes that led to the increase in lattice parameters. From Table 4.1, the intensity of the prominent peak increased up to 500 °C. The reduction of the relative peak intensity is attributed to the reduction of crystal quality (Ungula, Dejene, & Swart, 2017). The XRD results in Figure 4.2 at furnace temperatures of 300 °C, and 400 °C show that there are impurity phases of precursor materials at lower synthesis temperatures than 500 °C which may be attributed to the fact that the precursor did not achieve good ignition temperature (Rojas-Hernandez, Rodriguez, Rubio-Marcos, Serrano, & Fernandez, 2015).

Table 4.1: Summary of FWHM, intensity, and 2-theta values of the highest diffraction peaks for $CaAl_2O_4$: Eu^{2+}, Dy^{3+} phosphor synthesized at different furnace temperatures.

Temp. (^{0}C)	2-theta(deg)	Intensity (cps)	FWHM (deg)
300	19.877	515	0.12
400	19.92	392	0.18
500	29.582	1147	0.158
600	29.575	931	0.176
700	29.610	1403	0.165
900	29.698	1304	0.180
1000	29.508	1280	0.190

The crystallite size (D) of the product obtained was determined using Debye-Scherrer's equation (equation (4.1)) (Bertazzo & Bertran, 2006).

$$D = \frac{K\lambda}{\beta \cos\theta} \tag{4.1}$$

where β is the full width at half maximum (FWHM) broadening, θ is the Bragg's diffraction angle, K is the shape factor (0.9), D is the diameter of the crystallite, alongside λ is the emission wavelength of CuKα radiation (0.154 nm)(Farooqi & Srivastava, 2016)**.** The estimated crystalline size and other calculated values using equation (4.1) are shown in Table 4.2**.** The estimated crystalline size of the obtained phosphors was, 66.18, 44.12, 50.26, 45.12, 48.13, 44.12, and 41.80 nm for $CaAl_2O_4$: Eu^{2+}, Dy^{3+} synthesized at furnace temperatures of 300 °C, 400 °C, 500 °C, 600 °C, 700

°C, 900 °C and 1000 °C, respectively. From the data, it is seen that at a low furnace temperature of 300 °C, the particle size is big (66.18 nm) but reduces at a furnace temperature of 600 °C to 45.12 nm after which it increases again to 48.13nm at a furnace temperature of 700 °C.

Table 4.2: Summary of calculated values using equation (4.1) for $CaAl_2O_4$: Eu^{2+}, Dy^{3+} phosphor synthesized at different furnace temperatures.

Temp. (^oC)	K	λ (nm)	β (deg)	β (rad) (β*Π/180)	2Θ(deg)	Θ(deg)	Θ (rad) (Θ*Π/180)	D (nm)
300	0.9	0.154	0.12	0.0020944	19.877	9.9385	0.17345	66.18
400	0.9	0.154	0.18	0.0031416	19.92	9.96	0.17385	44.12
500	0.9	0.154	0.158	0.0027576	29.582	14.791	0.25815	50.26
600	0.9	0.154	0.176	0.0030718	29.575	14.7875	0.25809	45.12
700	0.9	0.154	0.165	0.0028798	29.610	14.805	0.25839	48.13
900	0.9	0.154	0.180	0.0031416	29.698	14.849	0.25916	44.12
1000	0.9	0.154	0.190	0.0033161	29.508	14.754	0.25751	41.80

The large crystal size means that the crystal has very low strain and dissolution while the small crystal size means that the crystal has high strain and dissolution (Rex, Nathan, & Vitalis, 2015). At a low furnace temperature of 300 °C, the gases escape slowly during synthesis making it difficult for the combustion to take place and hence low strain and dissolution (McKittrick, Shea, Sastry, & Bacalski, 1998). High synthesis temperature affects the crystallinity of the final product as the ignition occurs very fast leading to residual water during synthesis.

4.3.3. UV-Vis Analysis

The appraisal of the optical properties of the as-prepared $CaAl_2O_4$: Eu^{2+}, Dy^{3+} synthesized at furnace temperatures of 300 °C, 400 °C, 500 °C and 1000 °C were determined using aliquots drawn from freshly prepared samples using UV-Vis spectrophotometer. The data obtained was used to plot the graphs in Figure 4.3. From the graph, it is observed that the absorption intensity exhibited variations under synthesis temperature from 0.155 to 3.11¸that with 1000 °C being the lowest and 400 °C being the

highest. The sharp absorption edges also shifted to lower wavelengths with the increase of synthesis temperature. According to research done by (Anpo, Shima, Kodama, & Kubokawa, 1987), the particle size of a semiconductor material affects the UV absorption edge wavelength in a great way. The shifting of absorption edges to lower wavelengths could be attributed to size quantization(Li, White, & Lim, 2004),(Ranga Rao & Sahu, 2001).

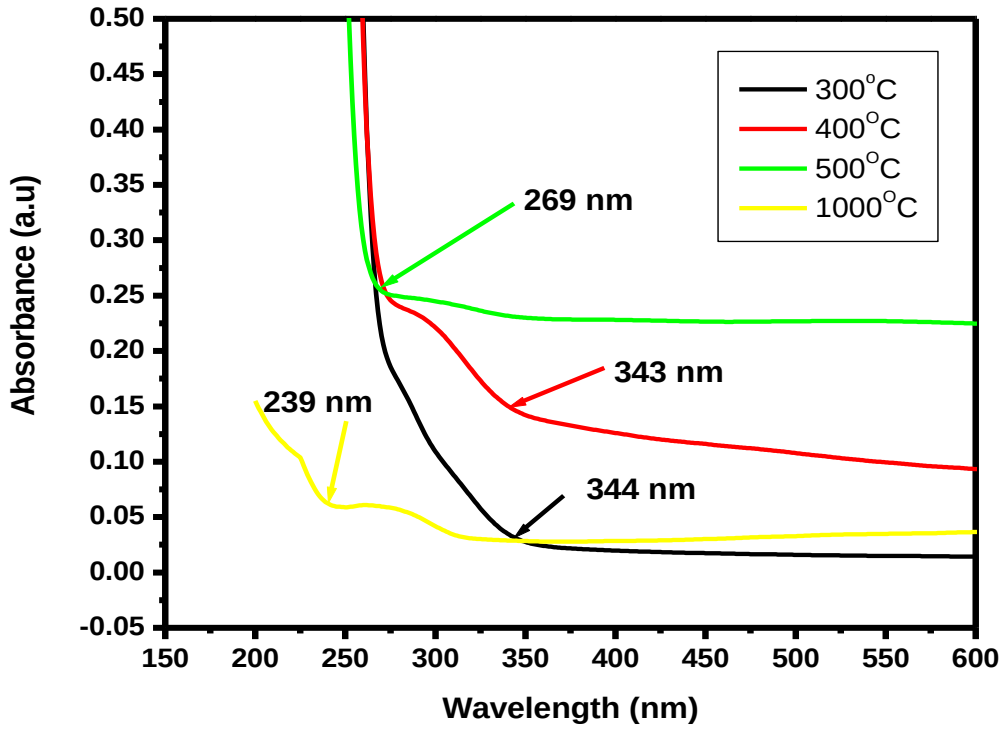

Figure 4.3: Absorption edges for $CaAl_2O_4$: Eu^{2+}, Dy^{3+}phosphor synthesized at different furnace temperatures.

To calculate the optical band gap energy of as-prepared $CaAl_2O_4$: Eu^{2+}, Dy^{3+} material, Tauc and Daviss-Mott relation (equation 4.2) (Makuła, Pacia, & Macyk, 2018) and Tauc plot (Figure 4.4) was used.

$$(\alpha h\nu)n = \mathrm{K}(h\nu - \mathrm{E}g) \qquad (4.2)$$

Where K is the energy-independent constant, Eg is the material's optical band gap energy, hν is the incoming photon energy, and α is the absorption rate coefficient. In the

above equation, the exponent "n" represent the nature of the transition (Sangiorgi, Aversa, Tatti, Verucchi, & Sanson, 2017).

For materials with a direct band gap, the power law exponent n is equal to 2, whereas for those with an indirect band gap, n is equal to 1/2. In the Tauc plot, the band gap energy was estimated by plotting $(\alpha h\nu)n$ against $h\nu$. Wavelength from the UV-Vis spectroscopy was converted to energy and the absorbance coefficient (α) was calculated from absorbance data. To get $(\alpha h\nu)n$plotted in the y-axis, $h\nu$was taken as incident photon energy and alpha (α) calculated from absorbance data using Beer-Lambert law (equation 4.3) (Swinehart, 1962).

$$\mathrm{I} = \mathrm{I}o e^{-\alpha \iota} \qquad (4.3)$$

Where I is the light's transmitted intensity, Io is the light's incident intensity, α is the absorbance coefficient and $\iota$is the length of the path of the light where absorbance occurred. On the curve, a tangent line where $\alpha = 0$ was then drawn and the location where it makes contact with the x-axis is taken as the optical band gap of the material.

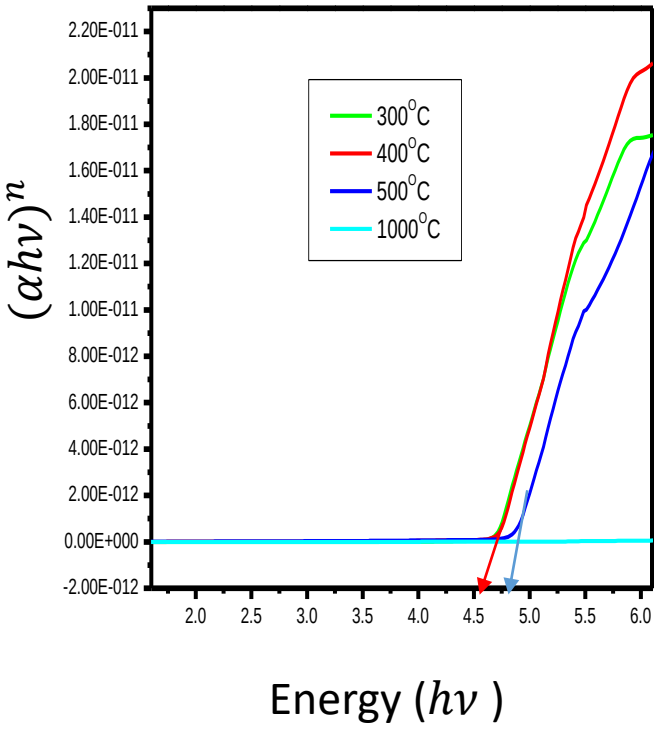

Figure 4.4: Tauc plot for $CaAl_2O_4$: Eu^{2+}, Dy^{3+} phosphor synthesized at different furnace temperature.

Table 4.3: A summary of Absorption edge and calculated values of Bandgap for $CaAl_2O$: Eu^{2+}, Dy^{3+} phosphor synthesized at different furnace temperatures.

Temperature (°C)	Absorption edge (nm)	Bandgap (eV)
300	270	4.6
400	266	4.7
500	263	4.8
1000	248	3.9

From the data above (Table 4.3), it is noted that the band gap increases with an increase in synthesis temperature up to 500°C but at a very high temperature of 1000 °C the band gap is very small (3.9 nm). This explains the good crystallinity of the samples synthesized at 500 °C because the atoms' vibrational energy weakens the interatomic spacing between them, requiring less energy to break the bond and facilitating the free migration of electrons to the conduction band, increasing the band gap value (Khaidir *et al*., 2019). the increase in the band gap shows that there is less delocalization and defects in the samples' structural system (Nazrin *et al*., 2018).

4.3.4. Scanning Electron Microscope Analysis

The SEM images of the as-synthesized$CaAl_2O_4$:Eu^{2+}, Dy^{3+} are shown in Figure 4.5. Figure 4.5 (a) shows the SEM image for $CaAl_2O_4$: Eu^{2+}, Dy^{3+} phosphor synthesized at a furnace temperature of 500 °C while Figure 4.5 (b) shows the SEM image for $CaAl_2O_4$: Eu^{2+}, Dy^{3+} phosphor synthesized at a furnace temperature of 1000 °C. The SEM micrographs (Figure 4.5) show that all the powders are agglomerated and are having irregular shapes with pores and cracks. The cracks and pores may be caused by the release of gases during combustion, which assist in the formation of nano-crystallite material as the sintering of the phosphor is avoided as a result of the dispersion of heat by escaping gases (Colen, 2015).The agglomerates have non-uniform sizes and shapes due to irregular mass flow and non-uniform distribution of temperature during synthesis.

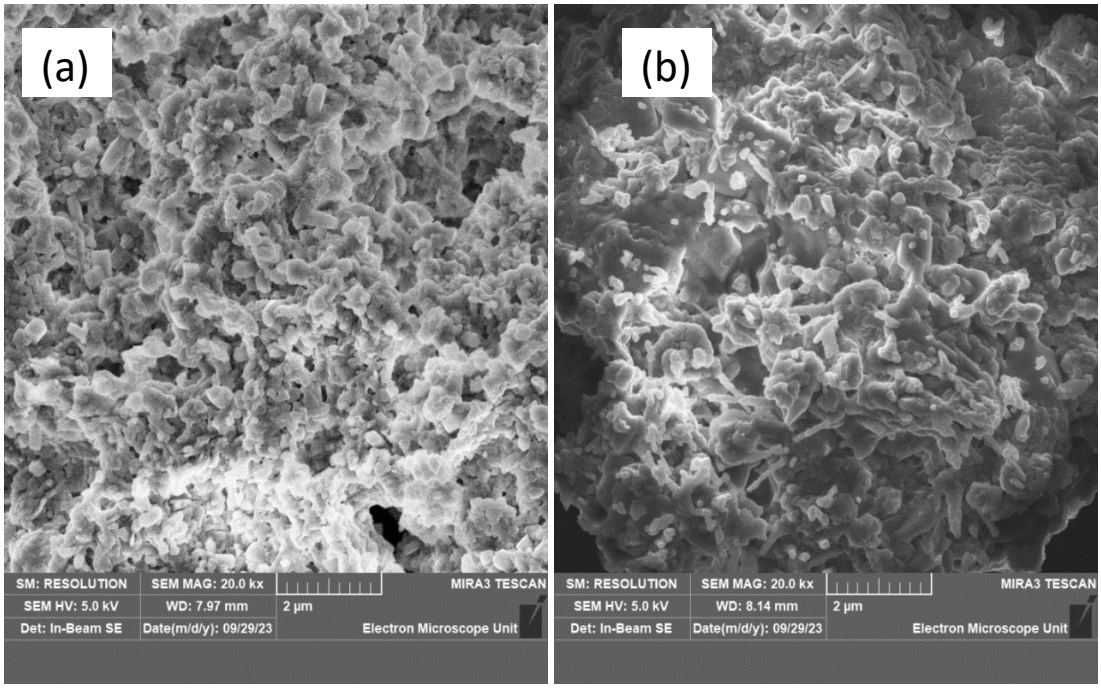

Figure 4.5: Representative SEM images for $CaAl_2O_4$: Eu^{2+}, Dy^{3+} phosphor synthesized at (a) 500 °C, and (b) 1000 °C.

The EDS results shown in Figure 4.6 (c) and Figure 4.6 (d) indicate that the elements of the phosphor for both samples are components of O, Al, and Ca indicating that the phase of final product was made of calcium aluminate. It can be seen that the atomic percentage of all the elements for $CaAl_2O_4$: Eu^{2+}, Dy^{3+} phosphor synthesized at a furnace temperature of 500°C. Figure 4.6 (c) is close to stoichiometric composition compared to that for $CaAl_2O_4$: Eu^{2+}, Dy^{3+} phosphor synthesized at furnace temperature of 1000 °C, Figure 4.6 (d). The change in the phosphor morphology is attributed to the escaping gases during the synthesis. At higher synthesis temperatures the functional group may be lost making atomic percentage of elements to be far from stoichiometric composition.

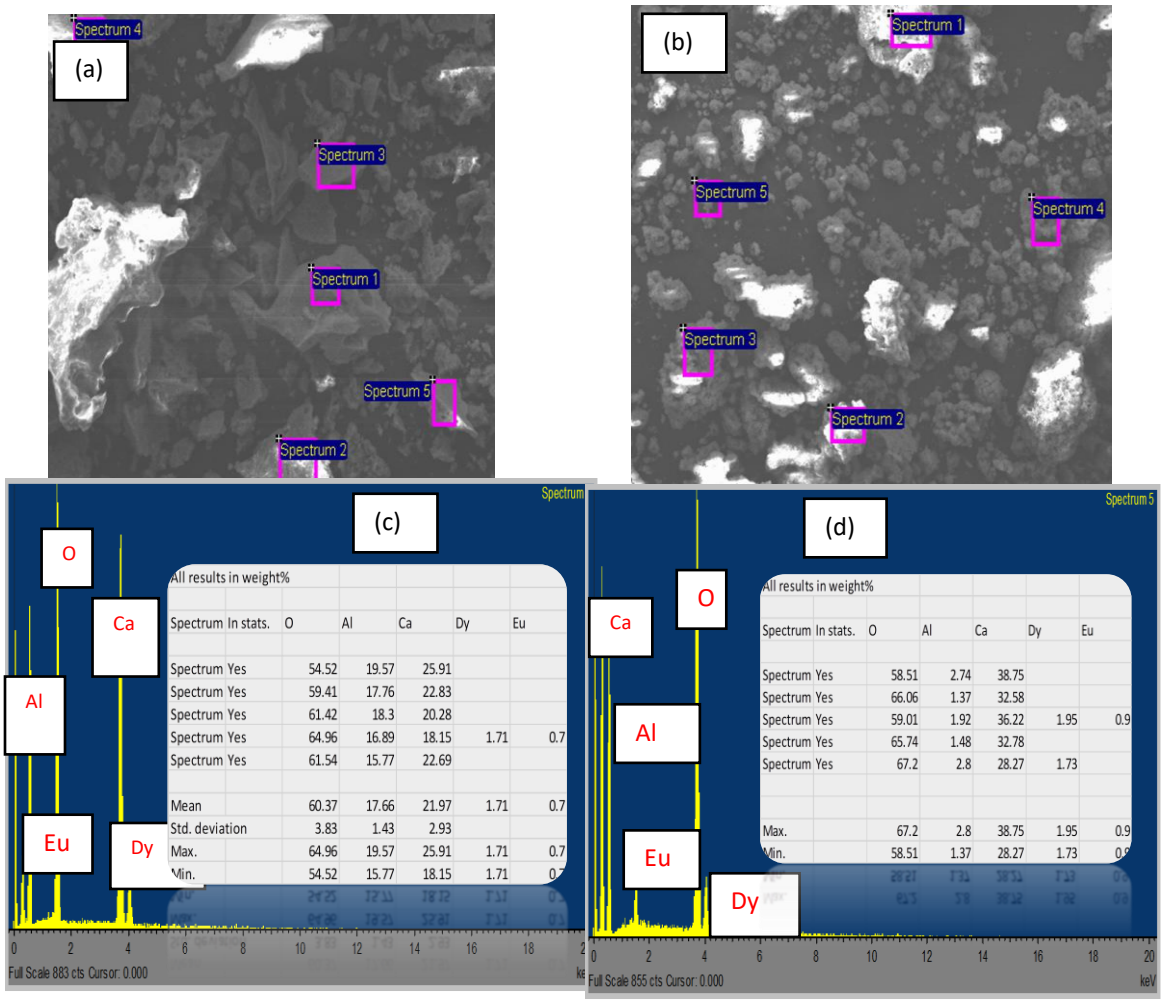

Figure 4.6: EDS spectra obtained from a point SEM analysis. (a) and (c) show the EDS results and spectrum for $CaAl_2O_4$: Eu^{2+}, Dy^{3+} phosphor synthesized at a furnace temperature of 500 °C; (b) and (d) present the EDS results and spectrum for $CaAl_2O_4$: Eu^{2+}, Dy^{3+} phosphor synthesized at a furnace temperature of 1000 °C.

4.4. Conclusion

The synthesis of $CaAl_2O_4$: Eu^{2+}, Dy^{3+} phosphor using the combustion method was successfully done. The as-prepared material's optical and structural characteristics of samples synthesized at different furnace temperatures were analyzed using FTIR, XRD, and UV-Vis spectroscopy. At both very high and low synthesis temperatures, the FTIR analysis of the final product produced the expected chemical combustion results with very few traces of $Ca_3Al_2O_6$ impurities. The X-ray diffraction (XRD) patterns exhibited a notable phenomenon where the diffraction angles of major peaks shifted towards higher 2theta values as the synthesis temperature increased. This was attributed to the

enlargement of particle dimensions, consequently leading to an expansion in lattice parameters. The intensity of the prominent peak demonstrated a noticeable increase up to 500°C, indicating an enhancement in crystal quality. Employing the Debye-Scherrer equation facilitated the determination of crystallite sizes, revealing temperature-dependent fluctuations. Analysis via UV-Vis spectroscopy unveiled a discernible downward trend in absorption edges as the synthesis temperature escalated. Notably, there was an observed widening of the band gap with increasing synthesis temperature up to 500 °C; however, at exceedingly high temperatures, such as 1000 °C, the band gap contracted significantly. (SEM) micrographs depicted the presence of agglomerated powders characterized by irregular morphologies, pores, and fissures. In summary, the investigation highlights that the optimal synthesis temperature of 500 °C yielded the most crystalline $CaAl_2O_4$: Eu^{2+}, Dy^{3+} phosphor, presenting itself as a promising candidate for deployment in lighting applications.

CHAPTER FIVE

EFFECTS OF pH ON THE STRUCTURAL AND OPTICAL PROPERTIES OF $CaAl_2O_4$: Eu^{2+}, Dy^{3+}NANOPARTICLES

5.1 Introduction

In contemporary research endeavors, there has been a pronounced emphasis on phosphors owing to their adaptability and applicability across various industrial domains, encompassing emergency guidance during intentional blackouts, in light emitting devices, fluorescence lamps, watches, demarcation of loads, and radiation dosimeter (Wako *et al*., 2014, 2016; Yen *et al*., 2018). Significant broad-spectrum emission extending across the electromagnetic spectrum from the deep blue to the red regions is typically displayed by phosphors doped with Eu^{2+} and Dy^{3+} (Haranath *et al*., 2007). $CaAl_2O_4$ is said to have a dominant hexagonal structure that remains unchanged even after doping from rare earth metal/lanthanide, Europium ion (Eu^{2+}) (Singh *et al*., 2016). The long-time used Sulphide phosphors are inferior to aluminate (Al_2O_4) phosphors doped with Eu^{2+} dopant (Wako *et al*., 2014). The dopant emits a broadband spectrum since the dopant undergoes electron transition from $4f^6\ 5d^1$ to $4f^7$ (Singh et al., 2016). This is because the excited Eu^{2+} ion is very unstable in a changed lattice structure (Wako *et al*., 2014).

Alkaline-earth aluminate phosphors exhibit long photoluminescence intensity for a long period and are chemically stable (Mao *et al.,* 2016), hence our interest in $CaAl_2O_4$:Eu^{2+} phosphor. It emits maximum spectra, blue in color, at 490-495nm as Eu^{2+} undergoes electron transition (Singh et al., 2016). However, co-doping done using other ions of the rare earth metal group leads to emission spectra within the green region at a maximum wavelength of 500 nm (Sakai *et al*., 1999, Bartwal and Ryu, 2008). The co-doping of $CaAl_2O_4$:Eu^{2+} phosphor with other ions of the rare earth metal group generates deeper traps, hence longer afterglow phosphorescence (Ryu *et al.,* 2008).

The host matrix and synthesis conditions affect the structural and optical properties of phosphors. pH affects the preferential precipitation of the phosphor at low pH for example, there is no complete combustion, and hence the Ca and Al will not be

completely precipitated giving rise to poorly developed crystal impurity alongside the pure crystal. In research done by (Shafia *et al*., 2014), on $SrAl_2O_4$: Eu^{2+}, Dy^{3+} phosphor, it was noted that at pH around 3-5, there was complete combustion, and pure crystal was formed. At very high pH, there was preferential precipitation of aluminum oxohydroxide in the precursor solution owing to the formation of impurities. It is worth noting that at neutral pH aluminum trihydroxide ($Al(OH)_3$ starts to precipitate and at certain conditions, water molecule was also lost from aliminium trihyroxide forming AlO(OH) leading to poor homogeneity and formation of suitable complex at high pH. The luminescence properties of phosphors are greatly influenced by pH. The excitation intensity slowly increases with increase in pH (Hsu & Lu, 2009). pH variation in a great extent affects the morphology of the sample which in turn affects the luminescence properties and hence affects the application suitability in different fields (Kumar et al., 2018). Although the phosphorescence of $CaAl_2O_4$:Eu^{2+} is known, information about the effect of different dopants and other synthesis conditions is scant. This study seeks to investigate the influence of pH on the structure and optical properties of $CaAl_2O_4$: Eu^{2+}, Dy^{3+} nanoparticles.

5.2 Experimental Procedure

The precursors were prepared with Ca/Al ratio kept constant according to the stoichiometric ratio. To investigate the effects of pH, ammonium carbonate $(NH_4)_2CO_3$ was added in different amounts to vary the pH of the solution. Five samples were prepared with pH of 2.9, 3.0, 3.4, 3.9, and 4.5. The doping concentrations of both Eu^{2+} and Dy^{3+} were kept constant at optimum concentration of 0.2 % mol and synthesized at a constant muffle furnace temperature of 500°C. Using a magnetic stirrer, the precursors were subjected to a 15-minute mixing protocol at ambient temperature to achieve uniformity and homogeneity within the solution. The solution boiled, then evaporated, and decomposed with the combustion causing the release of gases, including oxides of nitrogen, carbon, and ammonia, as well as smoke and fumes. After spontaneous ignition, combustion ensued, accompanied by significant swelling, and white foam was produced. The generated foam was allowed to cool to ambient temperature and milled to form the final product ($CaBaAl_2O_4$: Eu^{2+}, Dy^{3+}, Nd^{3+}).

The samples were further characterized by employing a variety of analytical methods. JEOL JSM-7500F field emission scanning electron microscope (FE-SEM) was used to explore the product particles' morphologies. The UV-Vis absorption spectra of the phosphor material were recorded using a Perkin-Elmer Lambda 750s UV-Vis spectrometer. The crystallinity and phase of the samples were examined using an X'Pert PRO PANalytical XRD diffractometer, utilizing Cukα radiation with a wavelength of λ = 0.15405 nm. to obtain the samples' X-ray diffraction (XRD) spectra. The consistency of the sample components and the type of bonds present was investigated using an FT-IR360 infrared spectrometer with KBr pellets, covering the spectral range from 4,000 to 400 cm^{-1}.

5.3. RESULTS AND DISCUSSION

5.3.1. Fourier Transform Infra-Red Analysis

Figures 5.1a, b, c, and d show the FTIR patterns of $CaAl_2O_4$: Eu^{2+}, Dy^{3+} synthesized at pH of 2.9, 3.0,3.9, and 4.5, respectively. In the spectral range from 420 cm^{-1} to 690 cm^{-1}, traces of $Ca_3Al_2O_6$ phase are detected (Wako, Dejene, & Swart, 2014). From Figure 5.1, a strong band at 1428.79 $cm^{-1}$for pH=2.9 in Figure 5.1a, 1432.58 cm^{-1} for pH=3.0, in Figure 5.1b, 1430.09 $cm^{-1}$for pH=3.9 in Figure 5.1c and 1421.65 cm^{-1} for pH=4.5 in Figure 5.1d. These bands are attributed to nitrate (NO_3^-) vibrations usually seen between 1250 cm^{-1} and 1650 cm^{-1} (Sahu et al., 2015).

The stretching vibration of AlO_4 is observed at 827.69 cm^{-1}, 810.17 cm^{-1}, 818.23 cm^{-1}, and 781.81 cm^{-1} for pH values 2.9, 3.0, 3.9, and 4.5, respectively, whereas the vibrational modes associated with the elongation of bonds in the metal oxide compounds Al-O, Ca-O, and Ca-O-Al bonds are seen at 573.63 cm^{-1} for pH = 2.9 in Figure 5.1a, 579.09 of cm^{-1} for pH = 3.0 in Figure 5.1b, 462.66 cm^{-1} and 571.18 cm^{-1} for pH = 3.9 in Figure 5.1 and 571.76 cm^{-1} for pH = 4.5. The absorption bands of AlO_4 are seen in the region between 680-500 cm^{-1} (Karacaoğlu, 2022). Absorption bands of 3704.39 cm^{-1} Figure 5.1 (c) and 3679.44 cm^{-1} Figure 5.1 (d) are associated with symmetric stretching vibration of water vapor absorbed by the samples from the atmosphere.

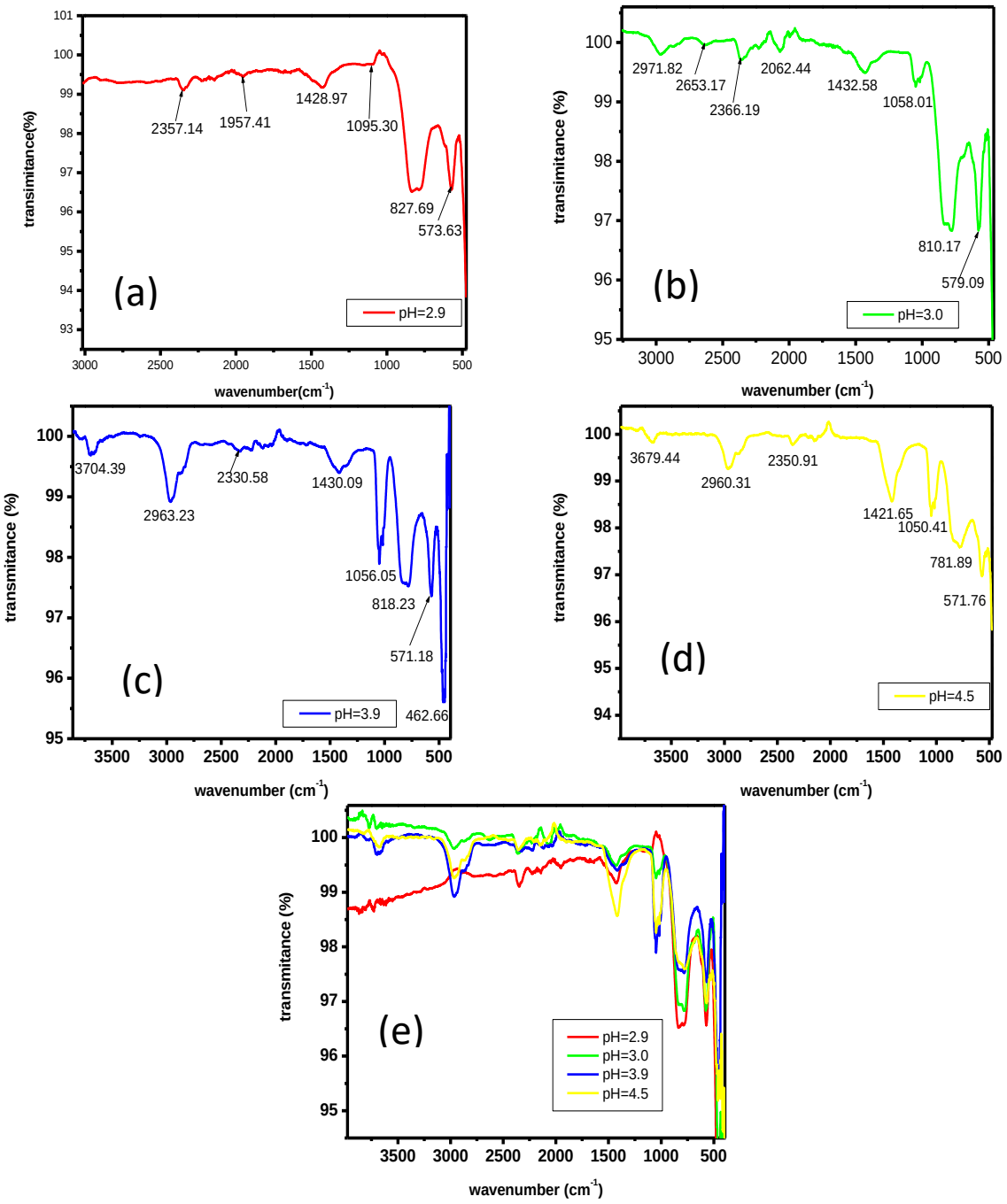

Figure 5.1: FTIR spectra of $CaAl_2O_4$: Eu^{2+}, Dy^{3+} synthesized at pH of (a) 2.9, (b) 3.0, (c) 3.9, (d) 4.5 and (e) for overplayed spectra.

5.3.2. X-ray diffraction Analysis

To acquire data concerning the crystalline characteristics lattice of as-prepared $CaAl_2O_4$: Eu^{2+}, Dy^{3+}, X-ray diffraction (XRD) assessments were done. The X-ray diffraction (XRD) data illustrating the patterns of $CaAl_2O_4$: Eu^{2+}, Dy^{3+} synthesized at pH of 2.9, 3.0,

3.4, 3.9, and 4.5 are illustrated in Figure 5.2. The powders' XRD patterns are dominated by the monoclinic phase diffraction peaks of $CaAl_2O_4$ and all the peaks are capable of being correlated with the characteristic monoclinic structure $CaAl_2O_4$ phase matching with the ICDD data file no.069-0033 for orthorhombic structure.

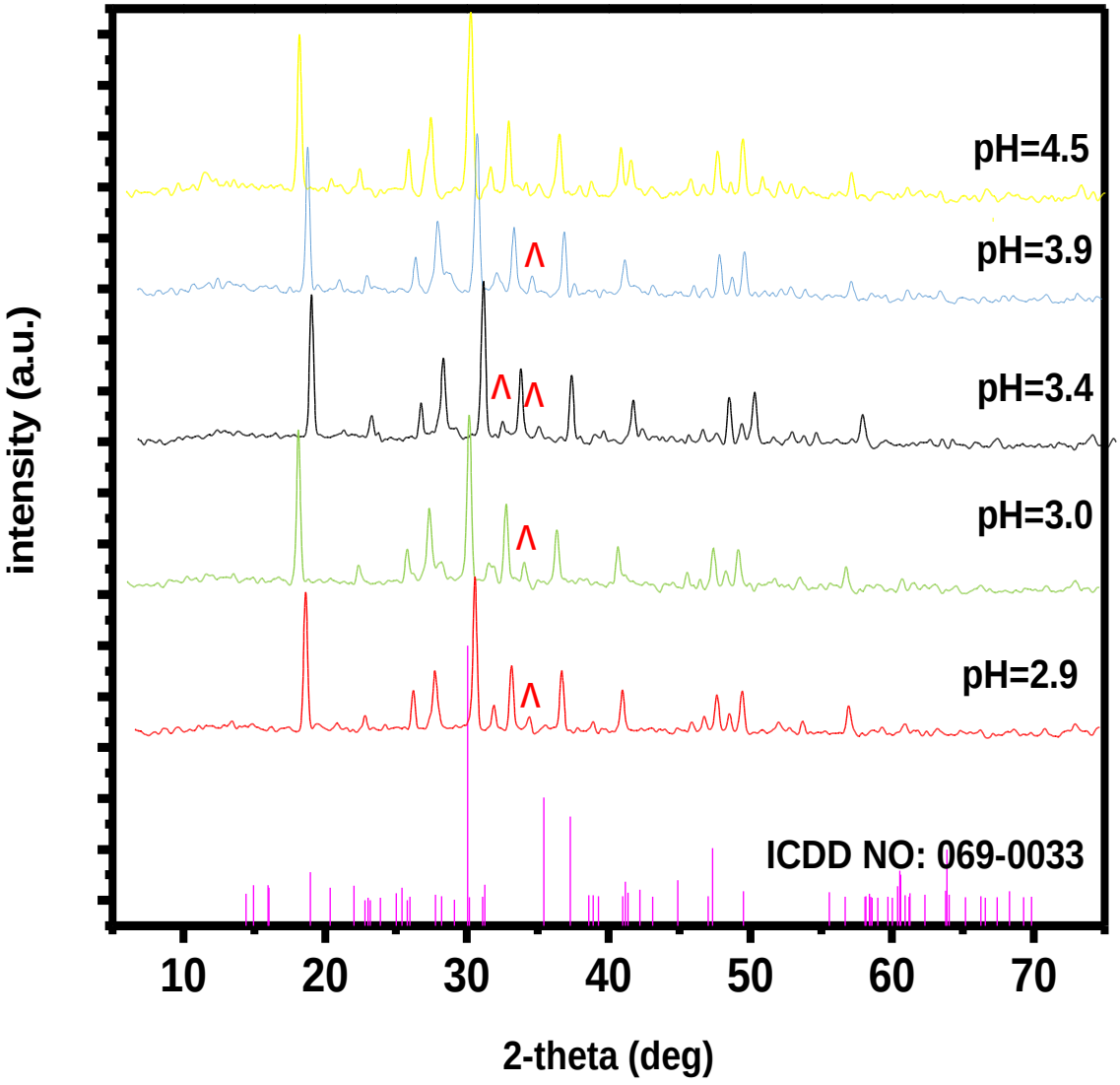

Figure 5.2: XRD patterns for $CaAl_2O_4$: Eu^{2+}, Dy^{3+} phosphor synthesized at different pH values.

From Figure 5.2 the XRD patterns show the presence of a few impurity phases (shown by red inverted v) at low pH (pH<3.9). Due to the inherent heterogeneity within the precursor mixture comprising urea and metallic ions, which subsequently leads to

inadequate combustion, preferential precipitation occurs in the starting mixture, causing this impurity phase(Shafia et al., 2014b). A similar observation was also noted by Hsu et al In their scientific inquiry into the influence exerted by pH levels on the kinetics of formation and the luminescent properties exhibited by sol-gel-derived $SrAl_2O_4:Eu^{2+}$, Dy^{3+} phosphor. They reported that there was the presence of impurity phases in samples prepared at low pH (pH<3) but the impurity phases reduced as the pH rose (Hsu & Lu, 2009b). As depicted in Figure 5.2 and detailed in Table 5.1, the diffraction angles of the predominant peaks exhibit a downward trend towards lower 2theta values across all samples, barring an anomaly observed in the sample synthesized under pH = 3.4, which demonstrates an opposite shift towards higher 2theta. Shifting the diffraction angle to a higher 2theta shows the presence of compressive stress while a lower 2theta shows the presence of tensile stress in the samples (Kumar et al., 2018). The sample synthesized under a pH condition of 3.0 demonstrated the most prominent intensity, quantified at 143 counts per second per degree, as elucidated in Table 5.1.

Table 5.1: Summary of FWHM, intensity, and 2-theta values of the highest diffraction peaks for $CaAl_2O_4$: Eu^{2+}, Dy^{3+} phosphor synthesized at different pH

pH	2-theta(deg)	Intensity (cps deg)	FWHM (deg)
2.9	33.686	140	0.147
3.0	33.604	143	0.18
3.4	33.811	128	0.170
3.9	33.702	130	0.276
4.5	33.701	133	0.152

The crystallite size (D) of the product obtained was determined using Debye-Scherrer's equation (equation (5.1)) (Bertazzo & Bertran, 2006).

$$D = \frac{K\lambda}{\beta \cos\theta} \tag{5.1}$$

where β is the full width at half maximum (FWHM) broadening, θ is the Bragg's diffraction angle, K is the shape factor (0.9), D is the diameter of the crystallite, while λ is the emission wavelength of CuKα radiation (0.154 nm)(Farooqi & Srivastava, 2016).

Table 5.2: Summary of calculated values using equation (1) for $CaAl_2O_4$: Eu^{2+}, Dy^{3+} phosphor synthesized at different pH

pH	β (deg)	β (rad)	2Θ(deg)	Θ(deg)	Θ (rad)		Aver. (nm)
		(β*Π/180)			(Θ*Π/180)	D(nm)	
2.9	0.147	0.002565634	33.686	16.843	0.293965806	56.44300958	46.13
	0.197	0.003438299	18.431	9.2155	0.160840817	40.83772822	
	0.200	0.003490659	30.070	15.035	0.262410253	41.11338749	
3.0	0.180	0.003141593	33.604	16.802	0.293250221	46.08515268	40.66
	0.187	0.003263766	18.373	9.1865	0.160334672	43.0180369	
	0.250	0.004363323	30.028	15.014	0.262043734	32.88747448	
3.4	0.170	0.00296706	33.811	16.906	0.295056637	48.82275442	50.12
	0.188	0.003281219	18.531	9.2655	0.161713482	42.79880173	
	0.140	0.002443461	30.150	15.075	0.263108385	58.74444083	
3.9	0.276	0.004817109	33.702	16.851	0.294105432	30.06330878	31.78
	0.231	0.004031711	18.427	9.2135	0.160805911	34.82678313	
	0.270	0.004712389	30.040	15.02	0.262148454	30.45222074	
4.5	0.421	0.007347836	33.702	16.851	0.294105432	19.70896253	29.59
	0.152	0.0026529	18.412	9.206	0.160675011	52.9264221	
	0.510	0.008901179	30.136	15.068	0.262986212	16.12539441	

The estimated crystalline size and other calculated values of most three intense peaks using equation (5.1) are shown in Table 5.2. The average estimated crystalline size of the obtained phosphors was, 46.13 nm, 40.66 nm, 50.12 nm, 31.78 nm, and 29.57 nm for $CaAl_2O_4$: Eu^{2+}, Dy^{3+} synthesized at pH of 2.9,3.0,3.4,3.9 and 4.5 respectively. The analysis of the data reveals that the estimated crystalline size of samples synthesized at acidic pH levels, particularly those below 3.9, is larger than that of samples synthesized at pH levels greater than 3.9. The large size of the crystal indicates the dimensions of the crystal has very low strain and dissolution while small size of the crystal indicates the dimensions of the crystal has high strain and dissolution which could be attributed to preferential precipitation of starting material in the product due to poor ignition at low

and high pH (Rex, Nathan, & Vitalis, 2015) the sample synthesized at pH equal to 4.5 had the smallest crystalline size and hence pH = 4.5 peaked as the best synthesis pH.

5.3.3. UV-Vis Analysis

The optical characteristics of the prepared sample $CaAl_2O_4$: Eu^{2+}, Dy^{3+} synthesized at pH of 2.9, 3.9, and 4.5 were determined for the aliquots drawn from the freshly prepared sample using UV-Vis spectrophotometer with excitation wavelengths ranging from 200nm to 500nm. The data obtained was used to plot the graphs in Figure 5.3.

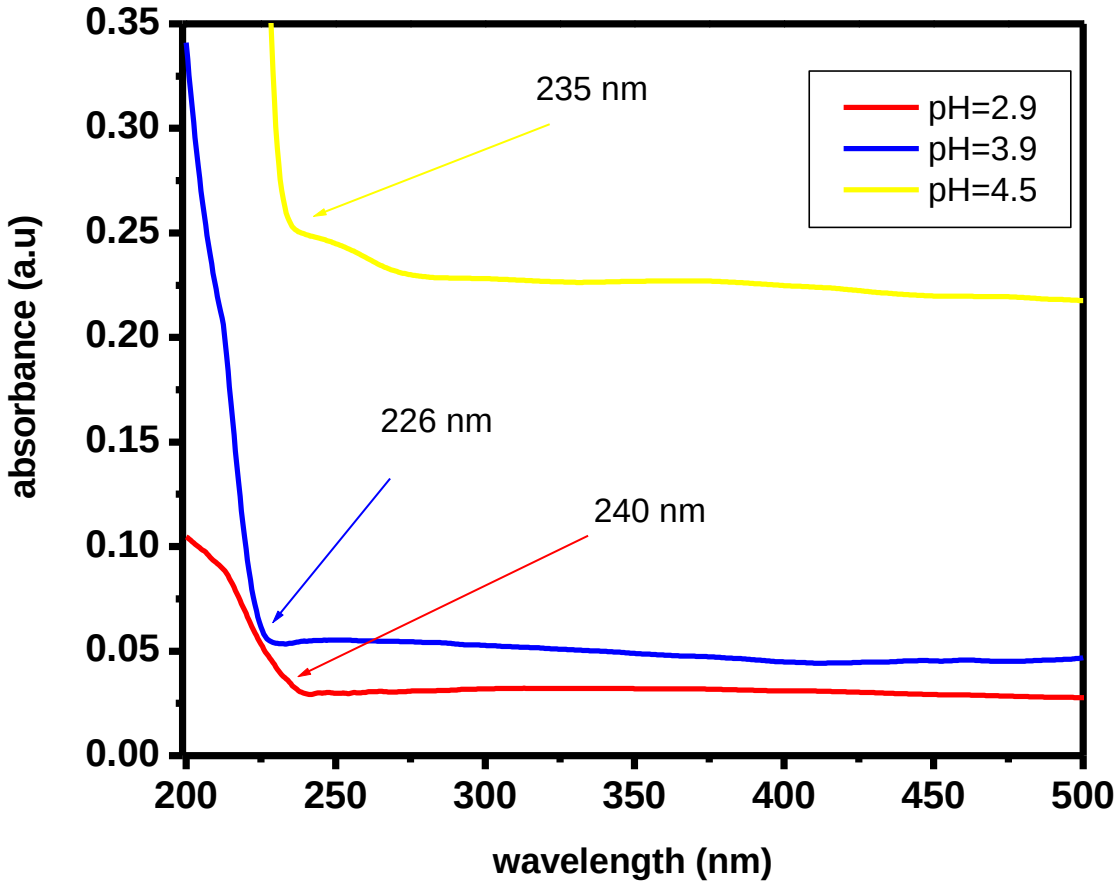

Figure 5.3: Absorption edges for representative samples of $CaAl_2O_4$: Eu^{2+}, Dy^{3+} phosphor synthesized at different pH values.

From the graph, it is evident that the distinct absorption edges shift with variations in pH, notably from pH 2.9 to pH 3.9 the absorption edge shift to lower wavelength while the absorption edge from pH 3.9 to pH 4.5 shifts to longer wavelength. The shifting of

absorption edge to lower or longer wavelength may be caused by change in pH hence slight lattice expansion (R. Liu et al.,2018).

To compute the optical band gap energy of the freshly synthesized $CaAl_2O_4$: Eu^{2+}, Dy^{3+} material, Tauc and Daviss-Mott relation (equation 5.2) (Makuła, Pacia, & Macyk, 2018)and Tauc plot (Figure 5.4) was used.

$$(\alpha h\nu)^n = \mathrm{K}(h\nu - \mathrm{E}g) \tag{5.2}$$

Where K is the energy independent constant, Eg is the material's optical band gap energy, hv is the incoming photon energy, and α is the absorption rate coefficient. In the above equation , the exponent " n" represent the nature of transition (Sangiorgi, Aversa, Tatti, Verucchi, & Sanson, 2017). For direct band gap, the value of n is 2, while for indirect band gap, the value is 1/2. In Tauc plot, the band gap energy was estimated by plotting$(\alpha h\nu)^n$ against $h\nu$. Wavelength from the UV-Vis spectroscopy was converted to energy and absorbance coefficient (α) calculated from absorbance data. To get $(\alpha h\nu)^n$ plotted in y-axis, $h\nu$ was taken as incident photon energy and alpha (α) calculated from absorbance data using Beer Lambert law (equation 5.3) (Swinehart, 1962)

$$\mathrm{I} = \mathrm{I}o e^{-\alpha \iota} \tag{5.3}$$

Where I is the light's transmitted intensity, Io is the light's incident intensity, α is the absorbance coefficient and ι is the length of the path of the light where absorbance occurred. On the curve, a tangent line where $\alpha = 0$ was then drawn and the location where it makes contact with the x-axis is taken as the optical band gap of the material.

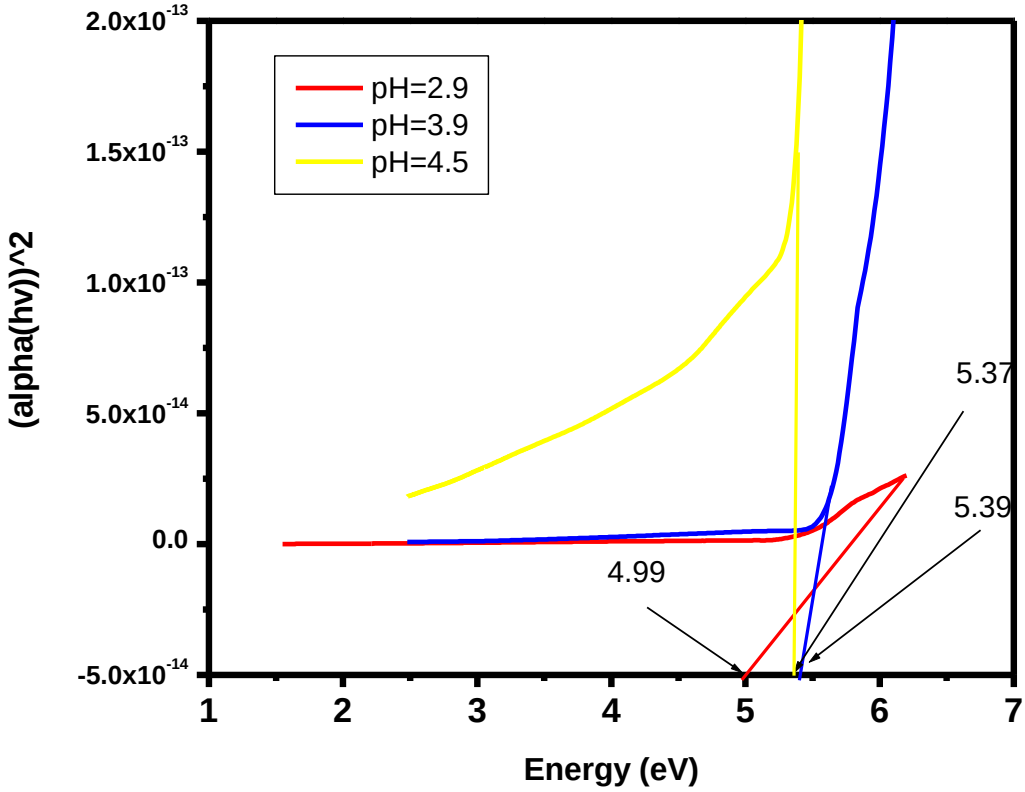

Figure 5.4: Tauc plot for $CaAl_2O_4$: Eu^{2+}, Dy^{3+} phosphor synthesized at different pH.

It is evident from Figure 5.4 and Table 5.3 that the band gap widens with the rise in pH, transitioning from pH = 2.9 (3.8) to pH = 4.5 (5.4). The increase in the band gap shows that there is less delocalization and defects in the samples' structural system (Khaidir et al., 2019). The sample synthesized at pH = 3.9 had a band gap of 5.0. Similar observations were reported by Kumar *et al.*, in their investigation concerning the adsorption of the hazardous dye methylene blue from aqueous solutions, employing combustion-derived $CaAl_2O_4$: Eu^{2+} (Kumara et al., 2016). It should be noted that the band gap of the sample synthesized under the pH condition of 4.5 had the largest band gap of 5.4 and hence admirable.

Table 5.3: A summary of Absorption edge and calculated values of bandgap using equation (5.2) for $CaAl_2O_4$: Eu^{2+}, Dy^{3+} phosphor synthesized at various pH levels.

pH	Absorption edge(nm)	Band gap (eV)
2.9	240	3.8
3.9	226	5.0
4.5	235	5.4

5.3.4. Scanning Electron Microscope Analysis

The SEM images of the as-synthesized $CaAl_2O_4$:Eu^{2+}, Dy^{3+} are shown in Figure 5.5. Figure 5.5(a) shows the SEM image for $CaAl_2O_4$: Eu^{2+}, Dy^{3+} phosphor synthesized at pH = 4.5 while Figure 5.5(b) shows the SEM image for $CaAl_2O_4$: Eu^{2+}, Dy^{3+} phosphor synthesized at pH=3.9. The SEM micrographs (Figure 5.5) show that the sample synthesized under the pH condition of 4.5 has a much smaller particle size, is less agglomerated, and has more cracks and poles compared to the sample synthesized under the pH condition of 3.9. The cracks and pores may be caused by the liberation of gases during combustion, which actively contributes to the formation of nano-crystallite material as the sintering of the phosphor is avoided as a result of the dispersion of heat by escaping gases (Colen, 2015). The agglomerates have non-uniform sizes and shapes due to irregular mass flow and non-uniform distribution of temperature during synthesis. This confirmed that the sample synthesized at pH=4.5 obtained better combustion than that synthesized at pH=3.9 and hence better morphology.

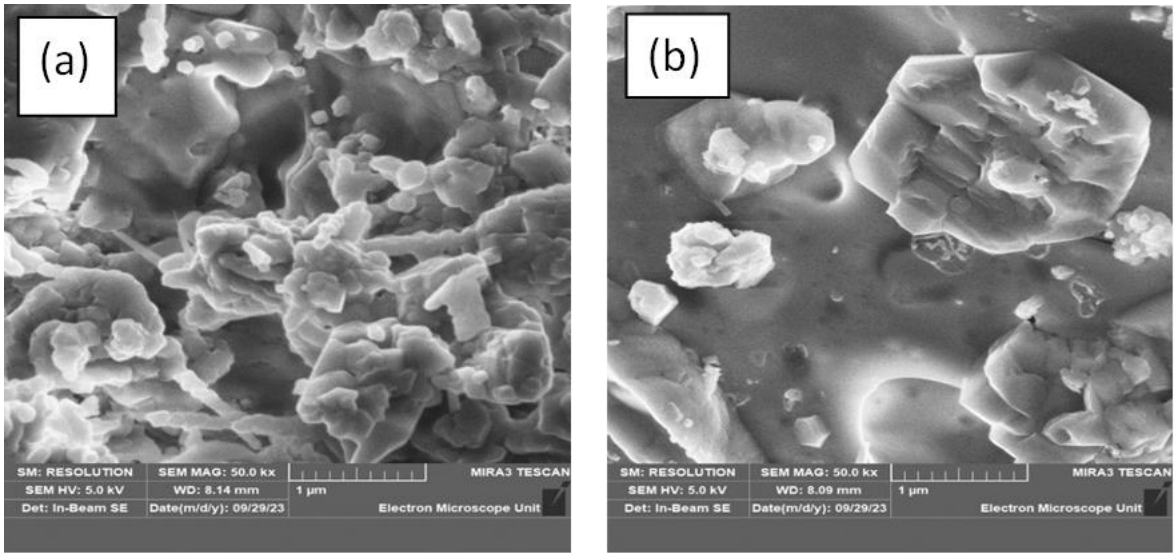

Figure 5.5: Representative SEM images for $CaAl_2O_4$: Eu^{2+}, Dy^{3+} phosphor synthesized at (a) pH = 4.5 and (b) Ph = 3.9.

Figure 5.6 shows the EDS results and a point spectrum for $CaAl_2O_4$: Eu^{2+}, Dy^{3+} phosphor synthesized at pH = 4.5. The EDS results shown in Figure 5.6 indicate that the elements of the phosphor for all samples are components of O, Al, and Ca indicating that the phase of the final product was made of calcium aluminate.

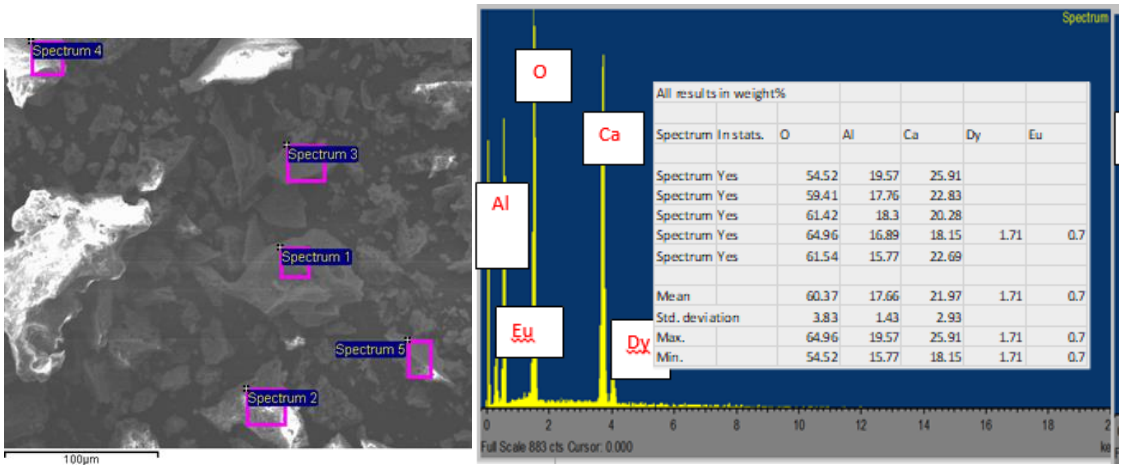

Figure 5.6: Representative EDS results from a point spectrum for $CaAl_2O_4$: Eu^{2+}, Dy^{3+} phosphor synthesized at pH = 4.5

5.4. Summary Conclusion

The synthesis of $CaAl_2O_4$: Eu^{2+}, Dy^{3+} phosphor using combustion method was successfully done. The inherent structural and optical attributes of the freshly synthesized samples at different pH were analyzed using FTIR, XRD and UV-Vis spectroscopy. Results from (XRD) spectroscopy conclusively affirmed the ubiquitous presence of the monoclinic phase within all examined samples. The final product's chemical combustion, with very little $Ca_3Al_2O_6$ impurity present at low pH, was as predicted by the Fourier-transform infrared analysis. At low pH, the XRD patterns reveal the existence of an impurity phase. Due to a lack of homogeneity between the urea and metallic ions in the precursor mixture, which results in poor combustion, preferential precipitation occurs in the starting mixture, causing this impurity phase. The major peak diffraction angles of all samples exhibit a pronounced downward shift in 2theta,apart from the sample synthesized under pH = 3.4, which demonstrates an anomalous upward shift in 2theta. Utilizing the Debye-Scherrer equation, the crystallite sizes of the samples in their nascent states were determined, revealing a discernible variability in crystallite dimensions corresponding to alterations in pH. Specifically, an intriguing observation emerges, indicating that the estimated crystalline size of samples synthesized under lower pH conditions (pH<3.9) exceeds that of samples synthesized under higher pH conditions (pH>3.9). Upon scrutinizing the UV-Vis spectra, conspicuous shifts in the sharp absorption edges are noted in tandem with variations in pH. Noteworthy is the discernible augmentation in band gap with escalating pH levels. Scanning electron microscopy analysis elucidates the agglomerated nature of all samples, typified by irregular morphology, replete with porous and fissured features. This comprehensive investigation underscores the pivotal significance of an optimal synthesis pH of 4.5 for $CaAl_2O_4$: Eu^{2+}, Dy^{3+} phosphor, yielding a superlative crystalline sample amenable for deployment in luminous applications.

CHAPTER SIX

INFLUENCE OF BARIUM AND NEODYMIUM DEFECTS IN THE HOST MATRIX ON THE STRUCTURAL AND OPTICAL PROPERTIES OF $CaAl_2O_4:Eu^{2+}, Dy^{3+}$ NANOPARTICLES

6.1. Introduction

Phosphors are solid materials that emit light, a phenomenon known as luminescence, and may also be a powder or a thin film(Rack & Holloway, 1998). This happens when they absorb ultraviolet, visible light, or thermal radiation. Luminescence is the emission of radiation in the visible region. Phosphors consist of a host matrix and dopants. The most common hosts are those of alkaline earth metals for example $CaAl_2O_4$, $BaAl_2O_4$, and $SrAl_2O_4$ while commonly used (Parauha, Sahu, & Dhoble, 2021) dopants are rare earth metals like europium (Eu) , dysprosium (Dy) and neodymium (Nd).

Following the unearthing of the Bologna stone in the nascent years of the 17th century, persistent luminescence was first described however, the specifics of the energy storage and gradual release are still poorly explained. Researchers have come up with some methods for the synthesis of (Calcium Aluminate) powders. The methods included and are not limited to chemical precipitation, hydrothermal synthesis, sol-gel method, and solid-state reaction. However, these methods have many limitations like high synthesis temperatures of around 1300 –1500 ºC additionally, it entails an extended processing duration. In addition, the phosphor produced by these methods has a big grain size, affecting the luminescent properties. Due to these limitations, combustion synthesis was used in this study. The combustion synthesis method is better Because of certain benefits such as a low processing temperature ranging between 500 °C and 600 °C and rapid synthesis. Similarly, This technique yields a grain size at the submicron level (Parauha et al., 2021). Furthermore, the combustion method is an energy-saving technique that is highly exothermic, and homogenous products are formed within a short time (Ugemuge, Parauha, & Dhoble, 2021).

Studies of phosphorescent materials have been done because of their wide applications In various fields like traffic safety, emergency signage, timekeeping mechanisms, fluorescent technologies, and ink formulations. $CaAl_2O_4$ is said to have a dominant hexagonal structure that remains unchanged even after doping with rare earth metal/lanthanide, Europium ion (Eu^{2+}). The long-time used sulphide phosphors are inferior to aluminate (Al_2O_2) phosphors doped with Eu^{2+} dopant (Wako et al., 2014). The dopant gives a broadband emission spectrum since the dopant undergoes an electronic transition from $4f^6\ 5d^1$ to $4f^7$(Mehare, Mehare, Swart, & Dhoble, 2022). This is because the excited Eu^{2+} ion is very unstable in a varying lattice structure (Chen, Hao, & Chen, 2022).

The composition of the precursor material and synthesis conditions plays a critical role in determining the structural and optical properties of phosphors. Temperature is one of the conditions that affect the properties of phosphors. When the temperature is increased, $CaAl_2O_4$: Eu^{2+}, Dy^{3+} phosphors will emit radiation through thermoluminescence (TL) which will occur at different regions of different temperatures. This is in close relation to its long persistent luminescence properties and properties of photostimulated luminescence. Besides electrons in these temperature traps can be re-trapped once more, which could lead to photostimulated persistent luminescence (He *et al.*, 2015).

Alkaline-earth aluminate phosphors exhibit high photoluminescence intensity for a long period and are chemically stable (Mindru et al., 2017). They emit blue color maximizing at 490-495 nm as Eu^{2+} undergoes electron transition (Singh *et al.*, 2016). However, co-doping with other ions of the rare earth metal group leads to emission spectra within the green region at a maximum wavelength of 500nm (Sakai *et al*., 1999, Bartwal *et al*., 2008). The co-doping of $CaAl_2O_4$: Eu^{2+}phosphor with other ions of the rare earth metal group also generates deeper traps, hence a longer duration of luminescence (Wako, 2011).

6.2. Experimental Procedure

To study the influence of Barium and Neodymium defects on the structure and optical properties of $CaAl_2O_4:Eu^{2+}$, Dy^{3+} nanoparticles, $Ba(NO_3)_2$ and $Nd(NO_3)_3.5H_2O$ were added to the mixture. The precursors were meticulously concocted through a series of scientific procedures and Ca/Al ratio was kept constant according to the stoichiometric ratio. The concentrations of Eu^{2+} and Dy^{3+} dopants were also consistently maintained at optimum concentration. The concentrations of Nd^{3+} / $Dy^{3+}$was kept constant at a ratio of 1:1 with different concentrations of $Ba(NO_3)_2$ starting from 10 mol %, 20 mol %,30 mol %,40 mol %, to 50 mol %. Using magnetic stirrer, the precursors were mixed for 15 minutes to obtain a homogeneous solution. Next, the solutions were transferred into crucibles and subsequently placed inside a muffle furnace and subjected to a furnace temperature of 500 °C.

The solution boiled, then evaporated, and decomposed with the combustion causing the release of gases, including oxides of nitrogen, carbon, and ammonia, as well as smoke and fumes. After spontaneous ignition, combustion ensued, accompanied by significant swelling, and white foam was produced. The generated foam was allowed to cool to ambient temperature and milled to form the final product ($CaBaAl_2O_4$: Eu^{2+}, Dy^{3+}, Nd^{3+}).

The samples were further characterized by employing a variety of analytical methods. JEOL JSM-7500F field emission scanning electron microscope (FE-SEM) was used to explore the product particles' morphologies. The UV-Vis absorption spectra of the phosphor material were recorded using a Perkin-Elmer Lambda 750s UV-Vis spectrometer. The crystallinity and phase of the samples were examined using an X'Pert PRO PANalytical XRD diffractometer, utilizing Cukα radiation with a wavelength of λ=0.15405 nm. to obtain the samples' X-ray diffraction (XRD) spectra. The consistency of the sample components and the type of bonds present was investigated using an FT-IR360 infrared spectrometer with KBr pellets, encompassing the spectral region ranging from 4,000 to 400 cm^{-1}.

6.3 Results and Discussion

6.3.1. Fourier Transform Infra-Red Analysis

Figure 6.1(a-f) shows the FTIR patterns of $CaBaAl_2O_4$: Eu^{2+}, Dy^{3+}, Nd^{3+} synthesized at different concentrations of $Ba(NO_3)_2$ starting from 10 mol % , 20 mol %, 30 mol %, 40 mol %, to 50 mol %, respectively. A strong band at 1413.03 cm^{-1} for 10 mol % in Figure 6.1(a), 1364.9 cm^{-1} for 20 mol % in Figure 6.1(b), 1362.3 cm^{-1} for 30 mol % in Figure 6.1(c),1360.31 cm^{-1} for 40 mol % in Figure 6.1d and 1334.83 cm^{-1} for 50 mol % in Figure 6.1(e) is attributed to nitrate (NO_3^-) vibrations usually seen in the region between 1250 cm^{-1} to 1650 cm^{-1} (Sahu et al., 2015). The stretching vibration of AlO_4 is detected at 875.51 cm^{-1}, 866.40 cm^{-1}, 891.73 cm^{-1}, 865.21 cm^{-1}, 849.69 cm^{-1} and 865.21 cm^{-1} for 10 mol % (Figure 6.1a), 20 mol % (Figure 6.1b), 30 mol % (Figure 6.1c), 40 mol % (Figure 6.1d) and 50 mol % (Figure 6.1e), respectively, while the stretching vibrations occurring in metal oxides of Al-O, Ba-O Ca-O, and Ca-O-Al bonds are seen at band of 720.33 cm^{-1} for 10 mol % (Figure 6.1a), 698.84 cm^{-1} for 20 mol % (Figure 6.1b), 711.66 cm^{-1} for 30 mol %, (Figure 6.1c), 605.66 cm^{-1} for 40 mol % (Figure 6.1d) and 712.91 cm^{-1} for 50 mol % (Figure 6.1e).

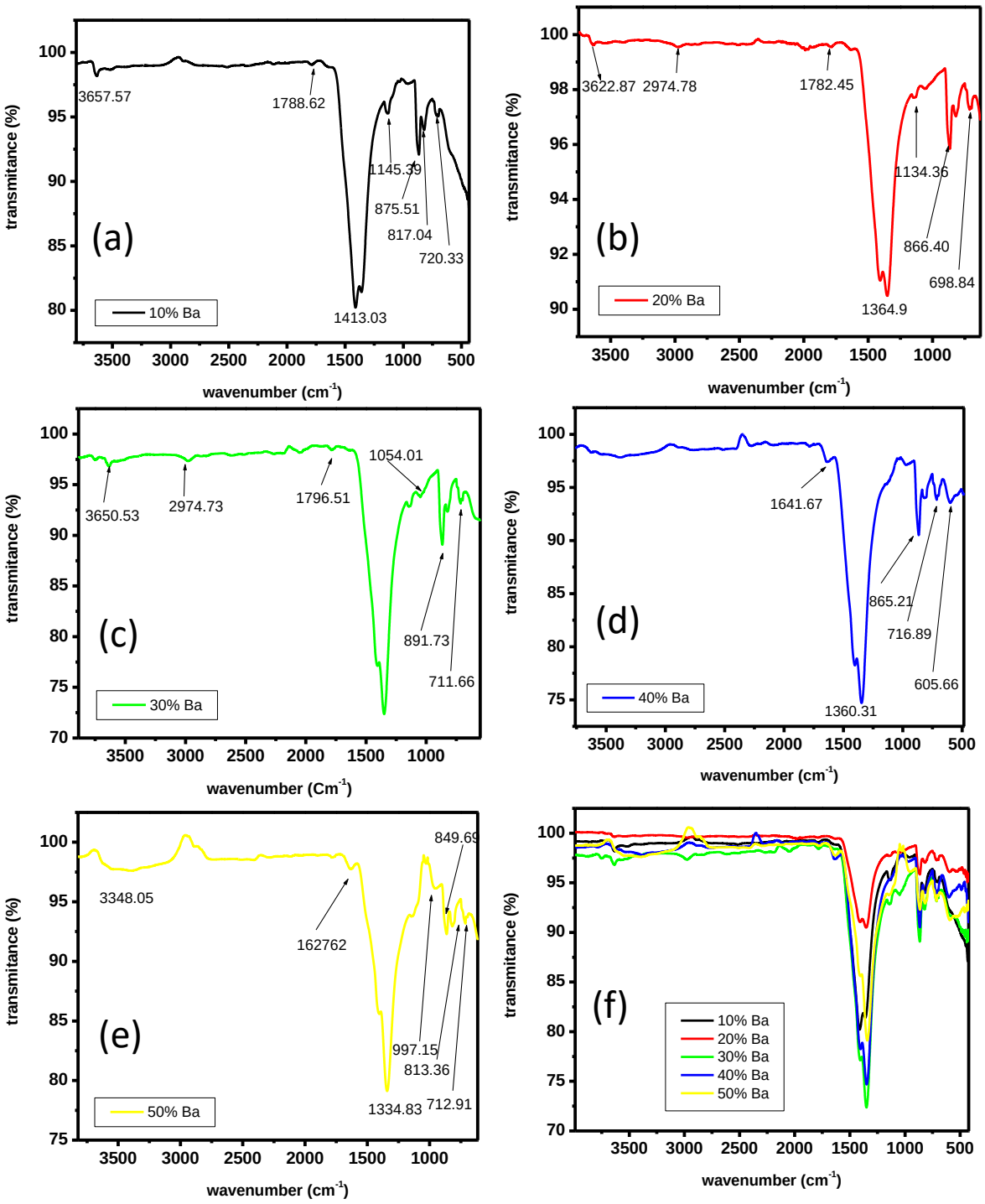

Figure 6.1: FTIR patterns of $CaBaAl_2O_4$: Eu^{2+}, Dy^{3+}, Nd^{3+} synthesized at different concentrations of $Ba(NO_3)_2$.

The absorption bands of AlO_4 are seen in the region between 680 -500 cm^{-1} (Karacaoğlu, 2022). The absorption band at 3657.57 cm^{-1} for 10 mol % (Figure 6.1a), 3622.87 cm^{-1} for 20 mol % (Figure 6.1b), 3650.53 cm^{-1} for 30 mol % (Figure 6.1c), broad bad at 3342.05 cm^{-1} for 40 mol % (Figure 6.1d) and broadband 3348.05 cm^{-1} for 50 mol % (Figure 6.1e) are associated to the symmetric stretching vibration of water vapor absorbed by the samples from atmosphere.

6.3.2. X-ray diffraction Analysis

To get information about the way atoms are organized in a crystal of as-prepared $CaBaAl_2O_4$: Eu^{2+}, Dy^{3+}, Nd^{3+}, (XRD) analysis was performed. The XRD spectra of $CaBaAl_2O_4$: Eu^{2+}, Dy^{3+}, Nd^{3+} synthesized at different concentrations of $Ba(NO_3)_2$ starting from 10 mol %, 20 mol %, 30 mol %, 40 mol %, to 50 mol %, respectively, are presented in the Figure 6.2. The powders' XRD patterns exhibit a predominant presence of monoclinic phase diffraction peaks of $CaAl_2O_4$, and all peaks can be attributed to the characteristic monoclinic phase of $CaAl_2O_4$ matching with the ICDD data file no.002-0852 for orthorhombic structure.

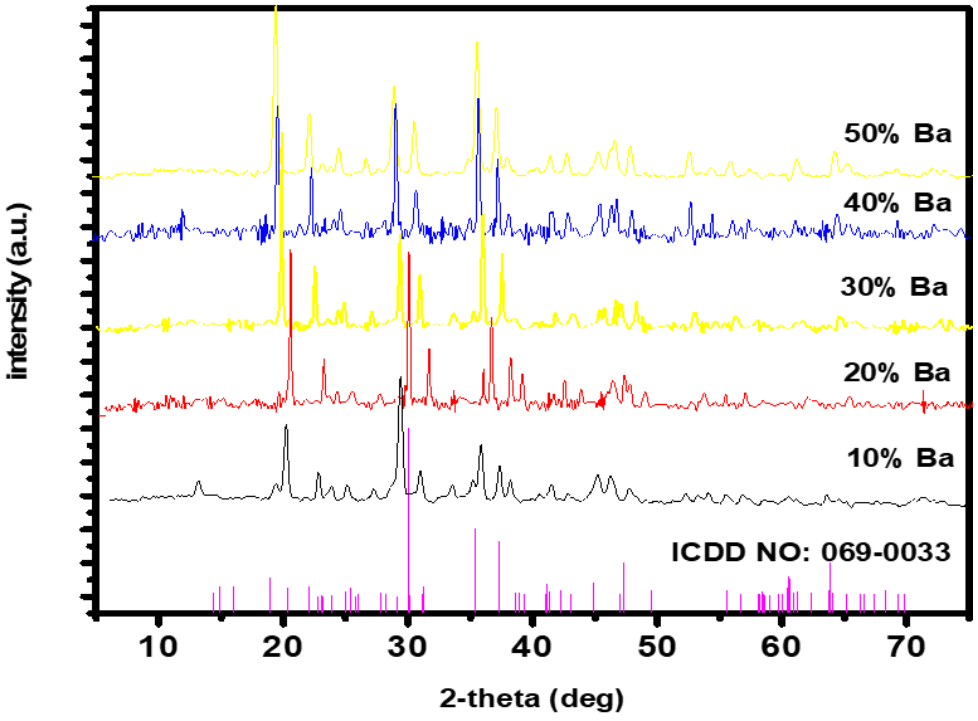

Figure 6.2: The XRD patterns of $CaBaAl_2O_4$: Eu^{2+}, Dy^{3+}, Nd^{3+} synthesized at different concentrations of $Ba(NO_3)_2$

From the XRD patterns Figure 6.2 and Table 6.1 it is seen that Apart from that of 20 % Ba, the major peaks' diffraction angles shift to lower 2theta. Introduction of alkaline earth metals with different ionic radii into the host matrix of $CaAl_2O_4$:Eu^{2+}, Dy^{3+}led to change in $CaAl_2O_4$:Eu^{2+}, Dy^{3+} lattice and hence shift of major peaks. Ba^{2+} has an ionic radius of 0.134 nm while Ca^{2+} has an ionic radius of 0.106 nm therefore when a small ion (Ca^{2+}) is substituted with a large ion (Ba^{2+}), lattice expansion will occur which in turn leads to a shift in the diffraction peaks to lower 2theta (Colen, n.d.) The sample synthesized at a Ba concentration of 50 % has the highest intensity (196) while the sample synthesized at Ba concentration of 40 % has the lowest intensity of 63 as shown in Table 6.1. Low intensity shows less crystallinity while high intensity shows more crystallinity.

Table 6.1: Summary of FWHM, intensity, and 2-theta values of the highest diffraction peaks of $CaBaAl_2O_4$: Eu^{2+}, Dy^{3+}, Nd^{3+} synthesized at different concentrations of $Ba(NO_3)_2$.

Ba concentration (%)	2-theta(deg)	Intensity (cps deg)	FWHM (deg)
10	29.60	168	0.23
20	29.78	112	0.179
30	19.35	137	0.151
40	19.33	63	0.20
50	19.21	196	0.144

The crystallite size (D) of the product obtained was determined using Debye-Scherrer's equation (equation (6.1)) (Bertazzo & Bertran, 2006) and tabulated in Table 2.

$$D = \frac{K\lambda}{\beta \cos\theta} \tag{6.1}$$

where β is the full width at half maximum (FWHM) broadening, θ is the Bragg's diffraction angle, K is the shape factor (0.9), D is the diameter of the crystallite, alongside λ is the emission wavelength of CuKα radiation (0.154 nm) (Farooqi & Srivastava, 2016)**.**

Table 6.2: Summary of calculated values using equation (1) of $CaBaAl_2O_4$: Eu^{2+}, Dy^{3+}, Nd^{3+} synthesized at different concentrations of $Ba(NO_3)_2$.

Ba con. (%)	β (deg)	β (rad) (β*Π/180)	2Θ(deg)	Θ(deg)	Θ (rad) (Θ*Π/180)	D (nm)	Average D(nm)
10	0.230	0.004014257	29.610	14.805	0.258395996	35.71255267	32.2525
	1.180	0.020594885	47.560	23.78	0.415039296	7.354193864	
	0.150	0.002617994	19.169	9.5845	0.167281082	53.69076339	
20	0.179	0.003124139	29.780	14.89	0.259879526	45.90568782	46.51187
	0.145	0.002530727	19.358	9.679	0.168930418	55.55771771	
	0.220	0.003839724	37.080	18.54	0.323584043	38.07221666	
30	0.151	0.00263545	19.348	9.674	0.168843152	53.34933244	44.16942
	0.220	0.00383972	37.090	18.545	0.32367131	38.07333109	
	0.200	0.00349066	29.780	14.89	0.259879526	41.0855906	
40	0.144	0.002513274	19.205	9.6025	0.167595241	55.93084835	57.8333
	0.154	0.002687807	37.019	18.5095	0.323051718	54.3791805	
	0.130	0.002268928	29.652	14.826	0.258762515	63.18987265	
50	0.230	0.00401426	37.110	18.555	0.323845843	36.42010183	38.6098
	0.200	0.00349066	19.370	9.685	0.169035138	40.28006499	
	0.210	0.00366519	29.781	14.8905	0.259888252	39.1292247	

The estimated crystalline size and other calculated values of most three intense peaks using equation (1) are shown in Table 6.2. The average estimated crystalline size of the obtained phosphors was, 32.25nm, 46.51nm, 44.17nm, 57.83nm, and 38.6nm for $CaBaAl_2O_4$: Eu^{2+}, Dy^{3+}, Nd^{3+} synthesized at Ba concentration of 10 mol %, 20 mol %, 30 mol %, 40 mol %, and 50 mol %, respectively. From the data, it is seen that the estimated crystalline size of samples synthesized at low Ba concentration (10 mol %) and high Ba (50 mol %) concentration was smaller than that of samples synthesized at Ba concentration between 20 mol % and 40 mol %. The large size of the crystal indicates the dimensions of the crystal have very low strain and dissolution while the small size of the crystal indicates the dimensions of the crystal has high strain and

dissolution could be attributed by a shift in the lattice caused by the additional of ions that have different ionic radii.

6.3.3. UV-Vis Analysis

Figure 6.3 shows absorption spectra of the as-prepared $CaBaAl_2O_4$: Eu^{2+}, Dy^{3+}, Nd^{3+} synthesized at different concentrations of $Ba(NO_3)_2$. Figure 6.3(a) shows the absorption spectrum at 10 % mol. barium concentration, Figure 6.3(b) shows absorption spectrum at 30 % mol. Barium concentration and absorption spectrum for 50 % mol barium concentration is shown in Figure 6.3(c). The Absorption intensity increases with an increase in barium concentration as shown in Figure 6.3(d).

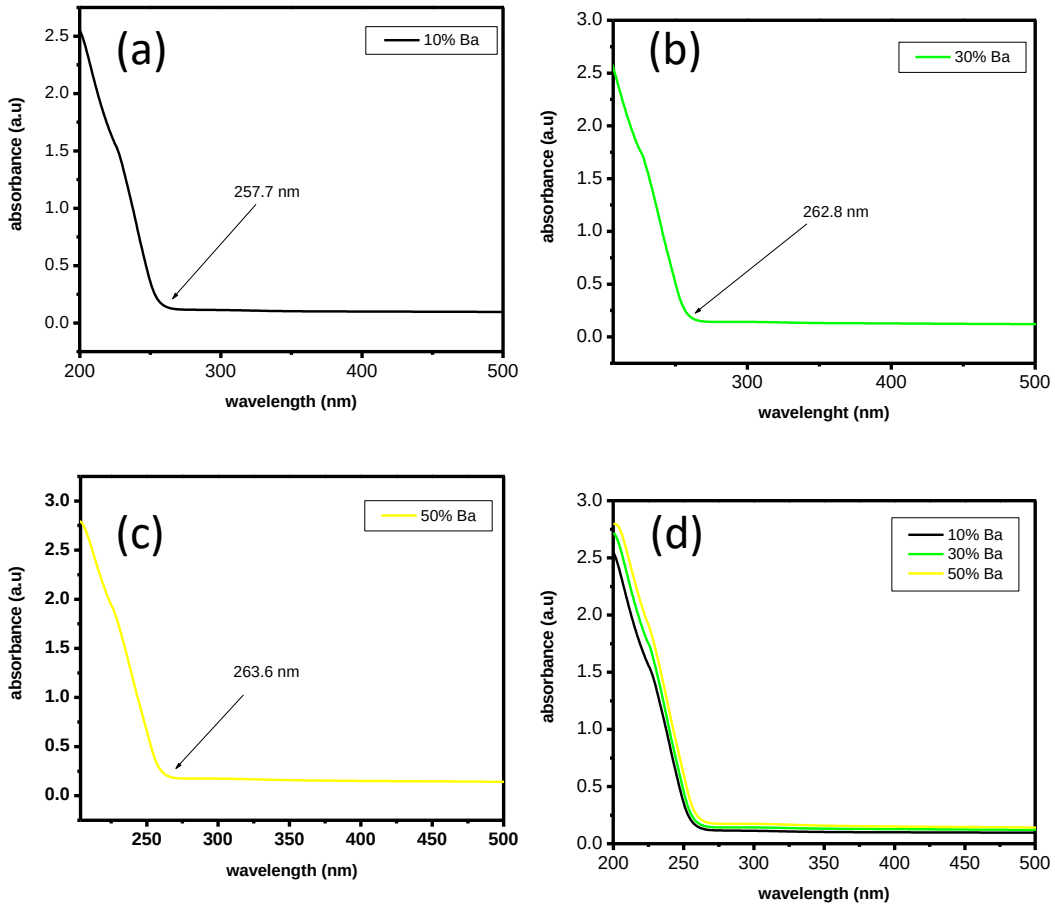

Figure 6.3: Representative absorbance spectra of the as-prepared $CaBaAl_2O_4$: Eu^{2+}, Dy^{3+}, Nd^{3+} synthesized at barium concentrations of (a)10 % mol, (b) 30 % mol and (c) 50 % mol.

An increase in absorption of photon energy causes an increase in absorption intensity as barium concentration increases. The absorption edge changes with a change in barium concentration. Expansion of lattice due to substitution of alkaline earth metal with small ionic radius with alkaline earth metal with larger ionic radius caused the shift of the absorption edge witnessed in Figure 6.3.

To calculate the optical band gap energy of as-prepare $CaAl_2O_4$: Eu^{2+}, Dy^{3+} material, Tauc and Daviss-Mott relation (equation 6.2) (Makuła, Pacia, & Macyk, 2018)and Tauc plot (Figure 6.4) was used.

$$(\alpha h\nu)n = \mathrm{K}(h\nu - \mathrm{E}g) \tag{6.2}$$

where K is the energy-independent constant, Eg is the material's optical band gap energy, hv is the incoming photon energy, and α is the absorption rate coefficient. In the above equation, the exponent "n" represent the nature of the transition (Sangiorgi, Aversa, Tatti, Verucchi, & Sanson, 2017)

For materials with a direct band gap, the index n equals 2, while for those with an indirect band gap, the index n equals 1/2. In Tauc plot, the band gap energy was estimated by plotting$(\alpha h\nu)n$ against$h\nu$. Wavelength from the UV-Vis spectroscopy was converted to energy and the absorbance coefficient (α) was calculated from absorbance data. To get $(\alpha h\nu)n$plotted in the y-axis, $h\nu$was taken as incident photon energy and alpha (α) calculated from absorbance data using Beer-Lambert law (equation 6.3) (Swinehart, 1962)

$$\mathrm{I} = \mathrm{I}o e^{-\alpha \iota} \tag{6.3}$$

Where I is the light's transmitted intensity, Io is the light's incident intensity, α is the absorbance coefficient and $\iota$is the length of the path of the light where absorbance occurred. On the curve, a tangent line where $\alpha = 0$ was then drawn and the location where it makes contact with the x-axis is taken as the optical band gap of the material.

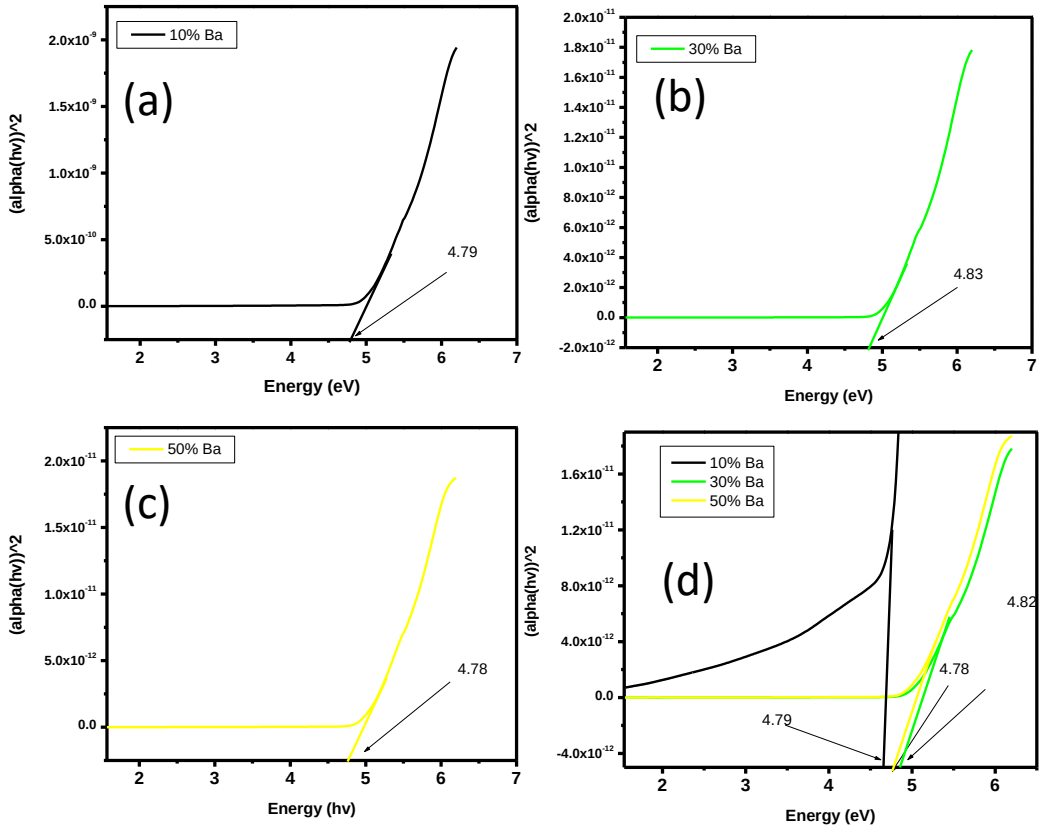

Figure 6.4: Tauc plot for $CaBaAl_2O_4$: Eu^{2+}, Dy^{3+}, Nd^{3+} synthesized barium concentration of (a) 10 % mol,(b) 30 % mol and (c) 50 % mol.

From Figure 6.4, it is seen that the band gap increased from 6.4 nm Figure 6.4 (a) to 4.83nm Figure 6.4 (b) with the increase in barium concentration from 10 % mol to 30 %. Burstein-Moss shift which happens as a result of the population state near the conduction band as barium concentration increases could be attributed to the increase in bad gap with an increase of barium concentration from 10% mol to 30 % mol(Society (TMS), 2013)when the barium concentration is further increased to 50 % mol, the band gap reduces to 4.78 as shown in 6.4 (c). At very high barium concentrations (50 %), a small energy level may be created in the band gap. This will lead to the formation of an impurity band below the conduction band and hence cause the shrinking of the band gap of the phosphor (T. Yang et al., 2022).

6.3.4. Scanning Electron Microscope Analysis

The SEM micrographs of the as-prepared $CaBaAl_2O_4$: Eu^{2+}, Dy^{3+}, Nd^{3+} synthesized at different concentrations of $Ba(NO_3)_2$ are seen in Figure 6.5. Figure 6.5 (a) shows SEM micrographs at 10 % mol. barium concentration while Figure 6.5 (b) shows SEM micrographs at 50 % mol. Figure 6.5's SEM micrographs demonstrate that all the powders are agglomerated and have irregular shape and cracks. Figure 6.5's SEM micrographs demonstrate that the sample was synthesized at 10 % mol. barium concentration has a much smaller particle size, smaller agglomerated, and has more cracks and poles compared to the sample synthesized at 50 % mol. barium concentration. The cracks and poles may be caused by the gases that escape during the combustion and aid in the formation of nano-crystallite material as the sintering of the phosphor is avoided as a result of the dispersion of heat by escaping gases (Colen, 2015). The agglomerates have non-uniform sizes and shapes due to irregular mass flow and non-uniform distribution of temperature during synthesis. The SEM images showed that the sample synthesized at 10 % mol had better morphology.

.

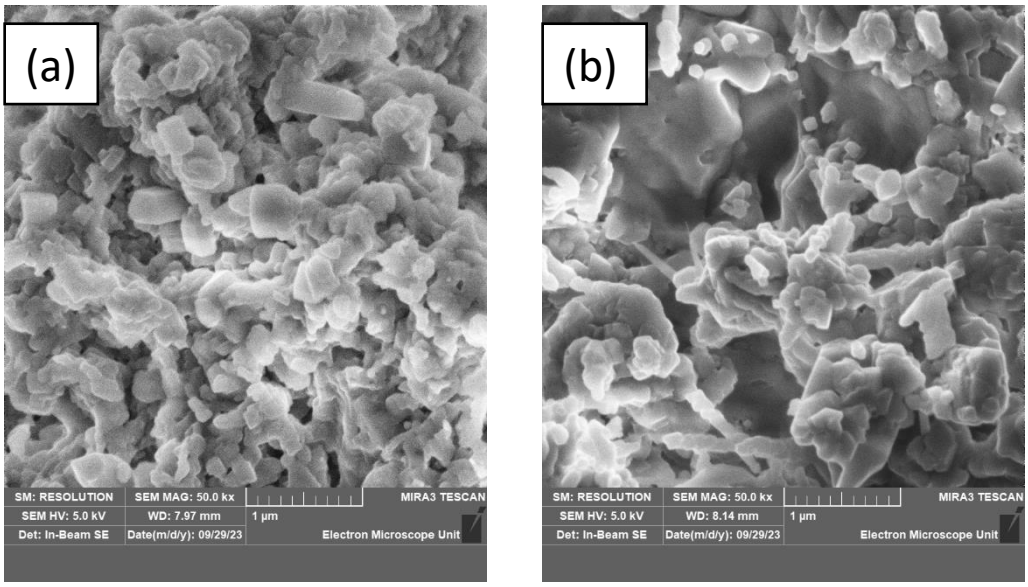

Figure 6.5: SEM micrographs of the as-prepare $CaBaAl_2O_4$: Eu^{2+}, Dy^{3+} , Nd^{3+} synthesized at barium concentration of (a) 10 % mol and (b) 50 % mol.

Figure 6.6 shows the EDS results from a point spectrum. Figure 6.6(a) and Figure 6.6 (c) show the EDS results and spectrum for$CaBaAl_2O_4$: Eu^{2+}, Dy^{3+}, Nd^{3+} phosphor synthesized at 10 % barium concentration while that in Figure 6.6 (b) and Figure 6.6 (d) shows the EDS results and spectrum for $CaBaAl_2O_4$: Eu^{2+}, Dy^{3+}, Nd^{3+} phosphor synthesized at 50 % barium concentration.

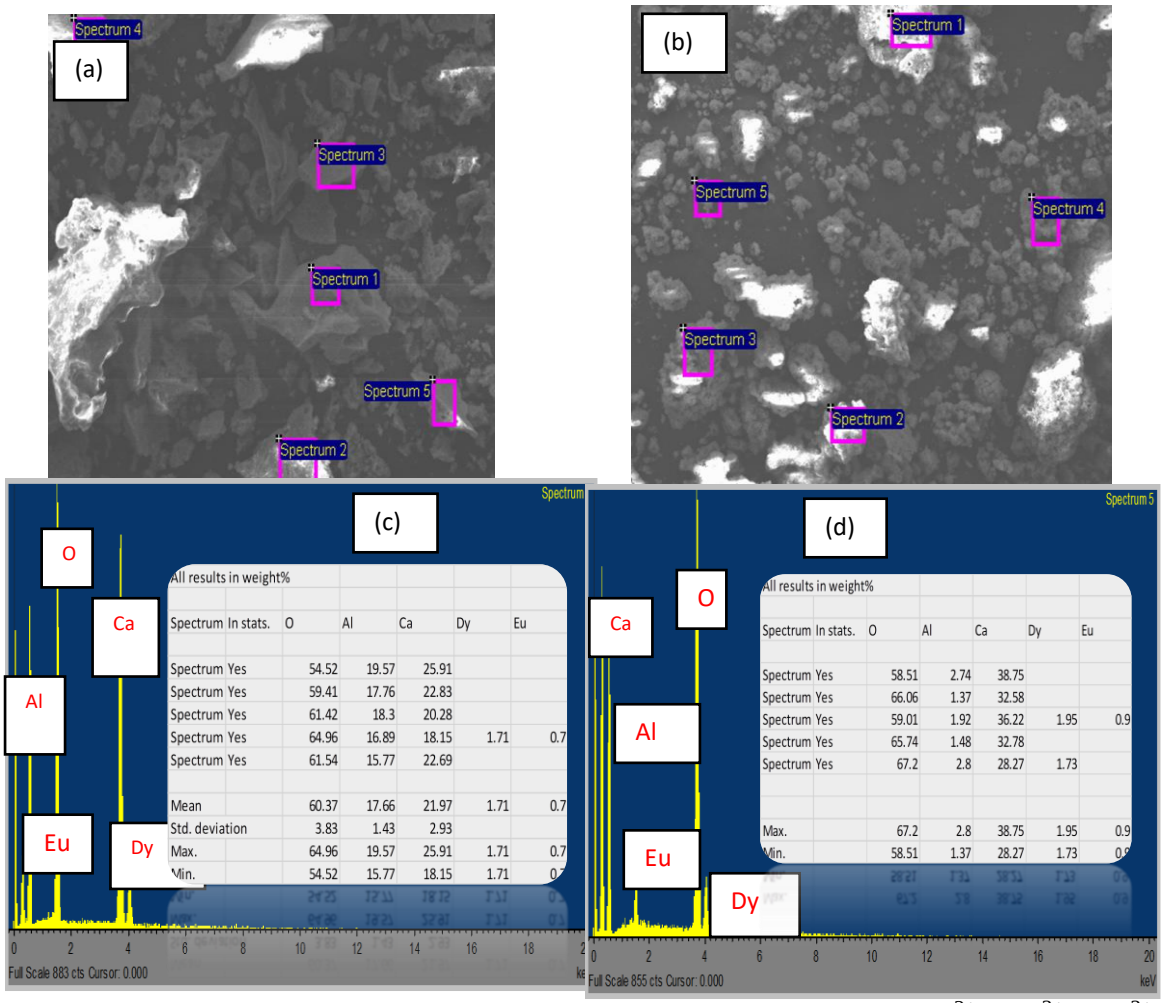

Figure 6.6: EDS results and a point spectrum for $CaBaAl_2O_4$: Eu^{2+}, Dy^{3+}, Nd^{3+} phosphor synthesized at (a) and (c) 10 % mol. barium concentration and (b) and (d) 50 % mol.

The EDS results, Figures 6.6 (d) and 6.6 (c), indicate that the elements in the phosphor for both samples consisted of O, Al, and Ca indicating that the phase of final product was made of calcium aluminate. The Nd and Dy intensities are less due to the small

concentration used during synthesis. C element is present in Figure 6(d) due to the carbon tape used in the sample holder.

6.4. Conclusion

The synthesis of $CaBaAl_2O_4$: Eu^{2+}, Dy^{3+}, Nd^{3+} phosphor using the combustion method was successfully done. The prepared samples' optical and structural characteristics synthesized at different concentrations of $Ba(NO_3)_2$ were analyzed using FTIR, XRD, and UV-Vis spectroscopy. The final product's anticipated chemical combustion results were provided by the FTIR analysis. The XRD patterns exhibited a shift in the diffraction angles of the major peaks to a lower 2θ, with the exception of the 20% Ba sample. Introduction of alkaline earth metals with different ionic radii into the host matrix of $CaAl_2O_4$:Eu^{2+}, Dy^{3+}led to change in $CaAl_2O_4$:Eu^{2+}, Dy^{3+} lattice and hence shift of major peaks. The proposed Debye-Scherrer formula was applied to ascertain the sizes of the crystallites of the samples in their prepared state. It was noted that there is variation in the crystallite sizes with changes in concentrations of $Ba(NO_3)_2$. As indicated by the UV-Vis graph, the Absorption, intensity increases with an increase in barium concentration, and the absorption edge changes with a change in barium concentration. The band separation was found to increase with an increase in barium concentration but at very high barium concentration the band gap is very small. The SEM micrographs show that all the powders are agglomerated and are shaped erratically and contain pores and cracks. The research shows that $CaBaAl_2O_4$: Eu^{2+}, Dy^{3+}, Nd^{3+}phosphor synthesized at barium concentration of 10%mol gave optimum concentration generating the most crystalline sample possible for use in lighting fixtures.

CHAPTER SEVEN

SUMMARY AND RECOMMENDATIONS

7.1 Summary

- The synthesis and characterization of $CaAl_2O_4$: Eu^{2+}, Dy^{3+} phosphor by combustion method was successfully done.
- An exploration into the impact of synthesis temperature, pH, and Barium defects on the structural and optical properties of $CaAl_2O_4$: Eu^{2+}, Dy^{3+} nanoparticles has been undertaken.

7.2 Conclusion

- Through utilization of various analytical techniques, it has been observed that modifications in the synthesis conditions induce alterations in both the structural configuration and optical behavior of the $CaAl_2O_4$: Eu^{2+}, Dy^{3+} nanoparticles. The study shows that $CaAl_2O_4$: Eu^{2+}, Dy^{3+} phosphor synthesized at 500°C, pH of 4.5, and barium concentration of 10%mol gave optimum synthesis conditions generating the most crystalline sample possible for use in lighting fixtures.

7.2 Recommendations for future work

- To study the effects of pH on the structure and optical properties of $CaAl_2O_4$: Eu^{2+}, Dy^{3+} nanoparticles should be done beyond a pH of 5.0.
- In forthcoming investigations, the exploration will delve into elucidating the impacts of different concentrations of barium on the structural morphology and optical behaviors of $CaAl_2O_4$: Eu^{2+}, Dy^{3+} nanoparticles beyond 50 %mol.

REFERENCES

Aitasalo, T., Hölsä, J., Jungner, H., Lastusaari, M., & Niittykoski, J. (2006). Thermoluminescence Study of Persistent Luminescence Materials: Eu^{2+}- and R^{3+}-Doped Calcium Aluminates, CaAl2O4:Eu2+,R3+. *The Journal of Physical Chemistry B*, *110*(10), 4589–4598. https://doi.org/10.1021/jp057185m

Baryshnikov, G., Minaev, B., & Ågren, H. (2017). Theory and Calculation of the Phosphorescence Phenomenon. *Chemical Reviews*, *117*(9), 6500–6537. https://doi.org/10.1021/acs.chemrev.7b00060

Bunaciu, A. A., Udriştioiu, E. gabriela, & Aboul-Enein, H. Y. (2015). X-Ray Diffraction: Instrumentation and Applications. *Critical Reviews in Analytical Chemistry*, *45*(4), 289–299. https://doi.org/10.1080/10408347.2014.949616

Campbell, A. K. (1988). *Chemiluminescence. Principles and applications in biology and medicine*. https://www.osti.gov/etdeweb/biblio/6603431

Chandan, V., Jain, M., Khadilkar, H., Charbiwala, Z., Jain, A., Ghai, S., Kunnath, R., & Seetharam, D. (2014). UrJar: A Lighting Solution using Discarded Laptop Batteries. *Proceedings of the Fifth ACM Symposium on Computing for Development*, 21–30. https://doi.org/10.1145/2674377.2674391

Chu, Y., Zhang, Q., Li, Y., Liu, Z., Xu, J., Zeng, H., & Wang, H. (2017). Hydrothermal synthesis of Bi4Ge3O12: Eu3+ phosphors with high thermal stability and enhanced photoluminescence property. *Journal of Alloys and Compounds*, *693*, 308–314.

Cirio, M., De Liberato, S., Lambert, N., & Nori, F. (2016). Ground State Electroluminescence. *Physical Review Letters*, *116*(11), 113601. https://doi.org/10.1103/PhysRevLett.116.113601

Colen, M. M. (2015). *Synthesis and characterization of long persistent phosphors using combustion method*. 121.

Dorenbos, P. (2005). Mechanism of Persistent Luminescence in Eu^{2+} and Dy^{3+} Codoped Aluminate and Silicate Compounds. *Journal of The Electrochemical Society*, *152*(7), H107. https://doi.org/10.1149/1.1926652

Ekambaram, S., Patil, K. C., & Maaza, M. (n.d.). *Synthesis of lamp phosphors: Facile combustion approach*. 13.

Gao, Y., Jing, Y., Liu, J., Li, X., & Meng, Q. (2017). Tunable thermal transport properties of graphene by single-vacancy point defect. *Applied Thermal Engineering*, *113*, 1419–1425.

Gillam, D. G., Khan, N., Maidan, N. J., & Barbe, P. M. (1999). Scanning electron microscopy (SEM) investigation of selected desensitizing agents in the dentine disc model. *Dental Traumatology*, *15*(5), 198–204. https://doi.org/10.1111/j.1600-9657.1999.tb00774.x

Hasnidawani, J. N., Azlina, H. N., Norita, H., Bonnia, N. N., Ratim, S., & Ali, E. S. (2016). Synthesis of ZnO Nanostructures Using Sol-Gel Method. *Procedia Chemistry*, *19*, 211–216. https://doi.org/10.1016/j.proche.2016.03.095

Hsu, C.-H., & Lu, C.-H. (2009a). Influence of pH on the formation and luminescence properties of the sol–gel derived $SrAl_2O_4$: Eu^{2+}, Dy^{3+} phosphors. *Advances in Applied Ceramics*, *108*(3), 149–154.

Hsu, C.-H., & Lu, C.-H. (2009b). Influence of pH on the formation and luminescence properties of the sol–gel derived $SrAl_2O_4$: Eu^{2+}, Dy^{3+} phosphors. *Advances in Applied Ceramics*, *108*(3), 149–154.

Huang, X., Sun, Q., & Devakumar, B. (2020). Facile low-temperature solid-state synthesis of efficient blue-emitting Cs3Cu2I5 powder phosphors for solid-state lighting. *Materials Today Chemistry*, *17*, 100288.

Karacaoğlu, E. (2022). Synthesis and Characterization of $CaAl_2O_4$: Dy^{3+} and $CaAl_2O_4$: Sm3+ Phosphor Powders. *El-Cezeri*, *9*(1), Article 1.

Kaya, S. Y., Karasu, B., Kaya, G., & Karacaoğlu, E. (2010). *Influences of Eu^{2+} and Dy^{3+} Contents on the Properties of Long Afterglow Strontium Aluminate Phosphors*. 88–94. https://doi.org/10.4028/www.scientific.net/AST.62.88

Kaygusuz, K. (2012). Energy for sustainable development: A case of developing countries. *Renewable and Sustainable Energy Reviews*, *16*(2), 1116–1126.

Kumar, A., Couto, M. H. M., Tiwari, S. P., Kumar, K., & Esteves da Silva, J. C. G. (2018). Effect of pH of Precursor on Up/Downconversion and Cathodoluminescence of Gd_2O_3:Ho^{3+}/Yb^{3+} Phosphor and Magneto-Optic Studies. *ChemistrySelect*, *3*(38), 10566–10573.

Kumara, B. P., Shivaprasada, K. H., Raveendrab, R. S., Krishnac, R. H., & Nagabhushanac, B. M. (2016). Adsorption of hazardous methylene blue from aqueous solution using combustion derived $CaAl_2O_4$ nanoparticles. *Journal of Materials Science & Surface Engineering*, *4*(7), 492–495.

Kuno, S., Akeno, H., Ohtani, H., & Yuasa, H. (2015). Visible room-temperature phosphorescence of pure organic crystals via a radical-ion-pair mechanism. *Physical Chemistry Chemical Physics*, *17*(24), 15989–15995.

Lakowicz, J. R. (1999). Introduction to Fluorescence. In J. R. Lakowicz (Ed.), *Principles of Fluorescence Spectroscopy* (pp. 1–23). Springer US.

McMullan, D. (1995). Scanning electron microscopy 1928–1965. *Scanning*, *17*(3), 175–185. https://doi.org/10.1002/sca.4950170309

Mohan, A. C., & Renjanadevi, B. (2016). Preparation of Zinc Oxide Nanoparticles and its Characterization Using Scanning Electron Microscopy (SEM) and X-Ray Diffraction(XRD). *Procedia Technology*, *24*, 761–766.

Park, S., & Vogt, T. (2010). Defect Monitoring and Substitutions in $Sr_{3-x}A_xAlO_4F$ (A = Ca, Ba) Oxyfluoride Host Lattices and Phosphors. *The Journal of Physical Chemistry C*, *114*(26), 11576–11583.

Picollo, M., Aceto, M., & Vitorino, T. (2019). UV-Vis spectroscopy. *Physical Sciences Reviews*, *4*(4).

Pifferi, A., Campi, G., Giacovazzo, C., & Gobbi, E. (2009). A New Portable XRD/XRF Instrument for Non-destructive Analysis. *Croat. Chem. Acta*, 6.

Qiao, Y., Zhang, X., Ye, X., Chen, Y., & Guo, H. (2009). Photoluminescent properties of Sr2SiO4:Eu3+ and Sr_2SiO_4:Eu^{2+} phosphors prepared by solid-state reaction method. *Journal of Rare Earths*, *27*(2), 323–326. https://doi.org/10.1016/S1002-0721(08)60243-4

Rodríguez Burbano, D. C., Sharma, S. K., Dorenbos, P., Viana, B., & Capobianco, J. A. (2015). Persistent and Photostimulated Red Emission in CaS:Eu^{2+},Dy^{3+} Nanophosphors. *Advanced Optical Materials*, *3*(4), 551–557.

Rosticher, C., Viana, B., Laurent, G., Le Griel, P., & Chanéac, C. (2015). Insight into $CaMgSi_2O_6$:Eu^{2+},Mn^{2+},Dy^{3+} Nanoprobes: Influence of Chemical

Composition and Crystallinity on Persistent Red Luminescence. *European Journal of Inorganic Chemistry*, *2015*(22), 3681–3687. https://doi.org/10.1002/ejic.201500257

Sahu, I. P., Bisen, D. P., Brahme, N., Tamrakar, R. K., & Shrivastava, R. (2015). Luminescence studies of dysprosium doped strontium aluminate white light emitting phosphor by combustion route. *Journal of Materials Science: Materials in Electronics*, *26*(11), 8824–8839. https://doi.org/10.1007/s10854-015-3563-5

Shafia, E., Bodaghi, M., Esposito, S., & Aghaei, A. (2014a). A critical role of pH in the combustion synthesis of nano-sized SrAl2O4:Eu2+, Dy3+ phosphor. *Ceramics International*, *40*(3), 4697–4706. https://doi.org/10.1016/j.ceramint.2013.09.011

Shafia, E., Bodaghi, M., Esposito, S., & Aghaei, A. (2014b). A critical role of pH in the combustion synthesis of nano-sized $SrAl_2O_4$: Eu^{2+}, Dy^{3+}, phosphor. *Ceramics International*, *40*(3), 4697–4706. https://doi.org/10.1016/j.ceramint.2013.09.011

Society (TMS), T. M., Metals &. Materials. (2013). *TMS 2013 142nd Annual Meeting and Exhibition: Annual Meeting, Supplemental Proceedings*. John Wiley & Sons.

Stefani, R., Rodrigues, L. C. V., Carvalho, C. A. A., Felinto, M. C. F. C., Brito, H. F., Lastusaari, M., & Hölsä, J. (2009). Persistent luminescence of Eu^{2+} and Dy^{3+} doped barium aluminate ($BaAl_2O_4$: Eu^{2+}, Dy^{3+}) materials. *Optical Materials*, *31*(12), 1815–1818. https://doi.org/10.1016/j.optmat.2008.12.035

Styrov, V. V., Tolmacheva, N. D., Tyurin, Yu. I., Shigalugov, S. Kh., Khoruzhii, V. D., Sivov, Yu. A., Plotnicova, E. Yu., & Sypchenko, V. S. (2014). On the heterogeneous chemiluminescence of Y_2O_2S crystal phosphors activated by europium. *Journal of Surface Investigation. X-Ray, Synchrotron and Neutron Techniques*, *8*(6), 1158–1160. https://doi.org/10.1134/S1027451014060147

Valeur, B., & Berberan-Santos, M. N. (2011). A Brief History of Fluorescence and Phosphorescence before the Emergence of Quantum Theory. *Journal of Chemical Education*, *88*(6), 731–738. https://doi.org/10.1021/ed100182h

Vlachos, N., Skopelitis, Y., Psaroudaki, M., Konstantinidou, V., Chatzilazarou, A., & Tegou, E. (2006). Applications of Fourier transform-infrared spectroscopy to edible oils. *Analytica Chimica Acta*, *573–574*, 459–465. https://doi.org/10.1016/j.aca.2006.05.034

Wako, A. H., Dejene, B. F., & Swart, H. C. (2014a). Roles of doping ions in afterglow properties of blue $CaAl_2O_4$: Eu^{2+}, Nd^{3+} phosphors. *Physica B: Condensed Matter*, *439*, 153–159. https://doi.org/10.1016/j.physb.2013.11.023

Wako, A. H., Dejene, F. B., & Swart, H. C. (2014b). Combustion synthesis, characterization and luminescence properties of barium aluminate phosphor. *Journal of Rare Earths*, *32*(9), 806–811. https://doi.org/10.1016/S1002-0721(14)60145-9

Wako, A. H., Dejene, F. B., & Swart, H. C. (2016). Structural and luminescence properties of $SrAl_2O_4$: Eu^{2+}, Dy^{3+}, Nd^{3+} phosphor thin films grown by pulsed laser deposition. *Physica B: Condensed Matter*, *480*, 116–124. https://doi.org/10.1016/j.physb.2015.09.049

Wako, M. A. H., Ed, B., Univ, H. E., & Ufs, B. H. (n.d.). *Preparation and Properties of Long Afterglow CaAl2O4 Phosphors Activated by Rare Earth Metal Ions*. 129.

Xue, F., Hu, Y., Fan, L., Ju, G., Lv, Y., & Li, Y. (2017). Cr^{3+} -activated $Li_5Zn_8Al_5Ge_9O_{36}$: A near-infrared long-afterglow phosphor. *Journal of the American Ceramic Society*, *100*(7), 3070–3079. https://doi.org/10.1111/jace.14874

Yan, X. L., Liu, Y. X., Yan, D. T., Zhu, H. C., Liu, C. G., & Xu, C. S. (2011). The Effects of Mn^{2+} Doping on the Luminescence Properties of $12CaO{\cdot}7Al_2O_3$:Eu^{2+} Nanocrystal Phosphor. *Journal of Nanoscience and Nanotechnology*, *11*(11), 9964–9969. https://doi.org/10.1166/jnn.2011.5292

Yang, S., Xiao, G., & Ding, D. (2021). Characterization and separation resistance of an in-situ 2D nanocarbon/calcium aluminate composite synthesized via a combustion method. *Journal of Asian Ceramic Societies*, *9*(3), 1038–1045. https://doi.org/10.1080/21870764.2021.1935122

Yang, T., Zhang, T., Huang, S., Christopher, T. D., Gu, Q., Sui, Y., & Cao, P. (2022). Structure tailoring and defect engineering of LED phosphors with enhanced thermal stability and superior quantum efficiency. *Chemical Engineering Journal*, *435*, 133873. https://doi.org/10.1016/j.cej.2021.133873

Yen, W. M., Shionoya, S., & Yamamoto, H. (2018). *Practical Applications of Phosphors*. CRC Press.

YU, Y., Wang, J., Wang, J., LI, J., ZHU, Y., Li, X., SONG, X., & GE, M. (2017). Structural characterization and optical properties of long-lasting $CaAl_2O_4$: Eu^{2+}, Nd^{3+} phosphors synthesized by microwave-assisted chemical co-precipitation. *Journal of Rare Earths*, *35*, 652–657. https://doi.org/10.1016/S1002-0721(17)60959-1

Zhou, W., Apkarian, R. P., Wang, Z. L., & Joy, D. (n.d.). *Fundamentals of Scanning Electron Microscopy*. 40.